Journal of Physical Oceanography

The DOI for this manuscript is doi: 10.1175/JPO-D-15-0008.1

The final published version of this manuscript will replace the preliminary version at the above DOI once it is available.

If you would like to cite this EOR in a separate work, please use the following full citation:

Thomas, L., J. Taylor, E. D'Asaro, C. Lee, J. Klymak, and A. Shcherbina, 2015: Symmetric instability, inertial oscillations, and turbulence at the Gulf Stream front. J. Phys. Oceanogr. doi:10.1175/JPO-D-15-0008.1, in press.

Symmetric instability, inertial oscillations, and turbulence at the Gulf Stream front

Leif N. Thomas *

Department of Environmental Earth System Science, Stanford University, Stanford, CA.

John R. Taylor

Department of Applied Mathematics and Theoretical Physics, University of Cambridge, Cambridge, UK.

Eric A. D'Asaro

Applied Physics Laboratory, University of Washington, Seattle, WA.

Craig M. Lee

Applied Physics Laboratory, University of Washington, Seattle, WA.

Jody M. Klymak

School of Earth and Ocean Sciences, University of Victoria, Victoria, British Columbia, Canada.

Andrey Shcherbina

Applied Physics Laboratory, University of Washington, Seattle, WA.

* *Corresponding author address:* Stanford University, 473 Via Ortega, Stanford, CA. 94305

E-mail: leift@stanford.edu

ABSTRACT

The passage of a winter storm over the Gulf Stream observed with a Lagrangian float and hydrographic and velocity surveys provided a unique opportunity to study how the interaction of inertial oscillations, the front, and symmetric instability (SI) shapes the stratification, shear, and turbulence in the upper ocean under unsteady forcing. During the storm, the rapid rise and rotation of the winds excited inertial motions. Acting on the front, these sheared motions modulate the stratification in the surface boundary layer. At the same time, cooling and down-front winds generated a symmetrically unstable flow. The observed turbulent kinetic energy dissipation exceeded what could be attributed to atmospheric forcing, implying SI drew energy from the front. The peak excess dissipation, which occurred just prior to a minimum in stratification, surpassed that predicted for steady SI-turbulence, suggesting the importance of unsteady dynamics. The measurements are interpreted using a large eddy simulation (LES) and a stability analysis configured with parameters taken from the observations. The stability analysis illustrates how SI more efficiently extracts energy from a front via shear production during periods when inertial motions reduce stratification. Diagnostics of the energetics of SI from the LES highlight the temporal variability in shear production, but also demonstrate that the time-averaged energy balance is consistent with a theoretical scaling that has previously been tested only for steady forcing. As the storm passed and the winds and cooling subsided, the boundary layer re-stratified and the thermal wind balance was reestablished in a manner reminiscent of geostrophic adjustment.

1. Introduction

The ocean's main frontal systems, the Gulf Stream, Kuroshio, and Antarctic Circumpolar Current, underlie the mid-latitude westerlies. As a consequence, the strongest wind-work on the ocean circulation is found in these regions (Wunsch 1998). At the same time, the westerlies tend to lower the potential vorticity of the currents and make the fronts susceptible to symmetric instability (SI), an overturning instability that removes kinetic energy (KE) from the circulation (Thomas 2005; Thomas et al. 2013). Under steady, unidirectional winds, theory and large eddy simulations (LES) predict that this sink of KE for the circulation scales with the so-called Ekman buoyancy flux, defined as the dot product of the Ekman transport and the surface buoyancy gradient (Thomas and Taylor 2010). Observations of upper-ocean turbulence made in the wind-forced Kuroshio when it was symmetrically unstable revealed enhanced turbulent dissipation at levels consistent with this theoretical prediction (D'Asaro et al. 2011).

While the findings are promising, extrapolating these results to estimate the global net sink of KE attributable to wind-forced SI might be ill-advised for several reasons. Principally, the conditions under which the theoretical prediction of Thomas and Taylor (2010) is formally applicable, i.e. steady, unidirectional winds, are rarely met in the ocean's main frontal systems. Here, the midlatitude westerlies coincide with the storm tracks and variable winds generate strong inertial motions (Alford 2003). How shifts in wind speed and direction and the resultant inertial motions affect the dynamics of symmetrically unstable fronts has not been investigated. A field campaign to the Gulf Stream during the late winter of 2012, described below, provided the ideal conditions to explore this physics. In this article we will focus on one particular storm event that generated a symmetrically unstable flow with pronounced time variability. After highlighting the key elements of the experiment and methods (section 2), we describe the evolution of the upper ocean during the passage of the storm (section 3) and then present a dynamical explanation by comparing the data with a LES (section 4) and simple stability analysis of a time-dependent, symmetrically unstable flow (section 5).

2. Experiment and measurements

The LatMix 2012 field campaign (February 19-March 17, 2012) studied submesoscale processes and their effect on mixing in the Gulf Stream and northern Sargasso Sea. For the work described here, two global class research vessels, the *R/Vs Knorr* and *Atlantis* surveyed around a subsurface, neutrally buoyant, acoustically tracked Lagrangian float (e.g. D'Asaro (2003)) which was deployed in the middle of the strong front ('North Wall') on the northern side of the Gulf Stream (see Fig. 1). The float was tracked using a Trackpoint-II short-baseline acoustic tracking system mounted on the *R/V Knorr*. Due to the deep mixed layers, acoustic ray paths remained near the surface for longer distances than in our previous summertime experiments allowing acoustic tracking of the floats at ranges of 5-6 km.

As in D'Asaro et al. (2011), the Lagrangian float provided a reference frame for the measurements. The float moved along the front at an average speed of about 1.4 m s^{-1}. However, there were considerable spatial variations in the flow moving away from the float. Specifically, the velocity was strongly sheared in the horizontal varying by $\sim \pm 0.5$ m s^{-1} within $\pm$5km of the track. Temperature and salinity measurements on the float show that the float remained in the front throughout the deployment. During this time, satellite IR images (not shown) illustrate that the front itself moves laterally about $\pm$15km, several times its own width. Thus by measuring relative to the float, the effects of both downstream and cross-stream advection were minimized, and changes in frontal properties could be interpreted as temporal changes in a Lagrangian reference frame moving along the axis of the front[1]. The vertical motion of the float within the boundary layer provided estimates of the turbulence intensity and dissipation rate (e.g. section 3c). The measurements were thus designed to study the properties of boundary layer turbulence within a strong front evolving in time.

Both vessels profiled velocity, salinity and temperature. Both used 300kHz and 75kHz underway ADCPs. Vertical sampling of the two vessels' ADCPs was identical, spanning the range between 15 and 87 m with 4-m bin size for 300kHz instruments and between 21.5 and 570 m with 8-m bin size for 75kHz ADCPs. One-minute ensemble averages were used, producing along-track resolution of about 0.2 km. Careful alignment of ADCP measurements was performed to minimize aliasing of ship speed into the measured velocities (Firing and Hummon 2010). A Triaxus towed, undulating profiler collected measurements from the R/V Knorr. Triaxus profiled from the sea surface to 250-m depth at vertical speeds of 0.8-1.0 m s^{-1} and typical tow speeds of 6-7 knots. The profiler carried an extensive payload of physical and bio-optical sensors, including a Seabird SBE 9 plus CTD equipped with dual, pumped temperature (SBE 3plus) and conductivity (SBE 4C) sensors sampled at 24 Hz. Comparisons of pre- and post-deployment laboratory calibrations showed no evidence of sensor drift. Differences in temperature and conductivity sensor response times introduce noise in the derived salinities. Corrections were thus applied for lags introduced by plumbing and by the thermal mass of the conductivity cell (Lueck and Picklo 1990; Morison et al. 1994). The corrected data were time-averaged to form 1 Hz time series, and, for the purposes of these analyses, further averaged into 2-m bins for both ascending and descending profiles, which themselves were subsequently averaged to create individual profiles. A Moving Vessel Profiler (MVP) was deployed from the *Atlantis*. The MVP (Rolls Royce MVP 200) is a weighted CTD that free-falls at approximately 3 m/s, and is returned to the surface by a winch. Casts to 200 m

[1]Realizing, however, that given the lateral shear in the current that measurements made away from the float are progressively less Lagrangian.

were recorded approximately every 800 m as the ship steams at 8 knots, and only down casts are used. The CTD data from the MVP is matched for temperature and conductivity cell response times.

This article focuses on data collected during a single float drift (March 5-9, yearday 64-68). Fig. 1 shows the tracks of the ships and float during this drift superimposed on an image of the sea surface temperature representative of the conditions at the time of these measurements. The *Knorr* made tight sections closely following the float while the *Atlantis* crossed a wider swath of the front so as to provide a larger-scale context. Both ships sampled hydrography at nominally 1 km resolution in the horizontal and less than 2 m in the vertical. The observations were made in the upper 200 m of the water column which was deep enough to capture both the surface boundary layer and the top of the pycnocline. Sections were completed on average every 1.3 hours on the *Knorr* and 3.3 hours on the *Atlantis* so that variability on time scales of an inertial period was well resolved. Note that since the water speeds (2 ms^{-1} was common) were comparable to the ship speeds and the sections are approximately perpendicular to the front in a frame advected with the flow, they are not perpendicular to the front in the geographical coordinate system presented in Fig. 1.

The sections were transformed into a streamwise coordinate system, where the downstream direction (with velocity component u and coordinate x), is defined as the speed-weighted average direction of the current on the section. The cross-stream coordinate y is defined to be perpendicular to the downstream direction, increases from the warm to cold side of the front, and is centered on the float. Once the streamwise coordinate was obtained, velocity and density data were mapped to cross-stream sections with a uniform grid by performing a one-dimensional cross-stream objective map at each vertical level. The form of the correlation function used in the mapping was Gaussian, with a RMS width of 1 km.

Air-Sea fluxes were estimated using *Knorr* shipboard meteorological measurements and the COARE 3.5 bulk formula (Edson et al. 2013) using the wind speed relative to the mean water velocity between 10 and 30m. The correction due to using the ocean currents averages -3.8%. The "3.5" modification of the COARE bulk stress calculation algorithm was developed from extensive direct wind stress observations during the Climate Variability and Predictability (CLIVAR) Mode Water Dynamic Experiment (CLIMODE; Marshall et al. (2009)) in the Gulf Stream system during wintertime – the region and the conditions nearly identical to those experienced during LatMix. The RMS accuracy of COARE 3.5 wind stress estimation is 28.9%, the best among all the COARE variants to date (Edson et al. 2013). Of the two available anemometers (port, starboard), the one least attenuated by the superstructure was chosen. The selection was based on the comparison of anemometer readings for various relative wind directions. The RMS difference in wind speed between the two instruments was 9% with a mean bias of 0.6%. The air-sea buoyancy flux was calculated from heat flux by multiplying the heat flux by the appropriate conversion factor (i.e. 6.0×10^{-10} m^4 s^{-3} W^{-1}). Neglecting buoyancy changes due to evaporation resulted in about 10% change in estimated buoyancy flux over yearday 65-66. Precipitation was negligible.

Strong and variable wind stress due to a rapidly moving low pressure system created a singular upper ocean response during the March 5-9 measurements (Fig. 1, 4a). The low pressure resulted in intense air-sea fluxes of heat and momentum. At the storm's peak the wind-stress exceeded 1 N m^{-2} and rotated clockwise in time, swinging from the northwest to the southeast. The clockwise rotary nature of the winds, their rapid time evolution, and their down-front component suggest that both inertial motions and SI could be present in the front. In the next section we describe observational evidence for both types of flows during the drift.

3. Evolution of the upper ocean within the Gulf Stream front

Sections of density and the downstream component of the vertical shear, $\partial u/\partial z$, from the *Atlantis* are presented in Fig. 2. The front is seen as a region of nearly uniform strong lateral gradient approximately centered on 0 km, the float location. The boundary layer, extending to approximately 40m (as determined by the vertical extent of the float's trajectory) with relatively weak stratification compared with the thermocline, nonetheless exhibits both vertical and horizontal density stratification (contours, lower panels), with vertical shear in the downstream velocity in the same sense as the thermal wind shear. The shear and stratification increase through yearday 65.35 (Fig. 2h) and then decrease rapidly so that by yearday 65.61 (Fig. 2j) both the vertical shear and vertical stratification have become weak. This event is the main focus of the analysis presented here.

Fig. 3 shows the evolution of stratification, $N^2 = \partial b/\partial z$ (where $b = -\sigma_\theta g/\rho_o$ is the buoyancy, σ_θ and ρ_o are the potential and reference densities, and g is the acceleration due to gravity), shear squared, $S^2 = (\partial u/\partial z)^2 + (\partial v/\partial z)^2$, and gradient Richardson number, $Ri = N^2/S^2$, following the float. Through yearday 65.4, the boundary layer is stably stratified ($N^2 \approx 3\times 10^{-5} s^{-2}$) except in the upper 10m. The float trajectory (Fig. 3 white/grey trajectories) repeatedly cycles across this indicating that active mixing is occurring to about 40m depth. The Richardson number (Fig. 3c) is less than 1, but larger than 0.25. From yearday 65.4 to 65.6, the stratification and shear rapidly decrease to establish an unstratified, unsheared boundary layer. The float trajectories repeatedly traverse this layer showing that active mixing extends to about 80m. The Richardson number remains near 1, except in the upper 20m where the density is unstable. This pattern persists to about yearday 66.2; over the next day the stratification and shear increase, with much weaker mixing and a shallowing mixed layer. A stratified, actively mixing boundary layer with a Richardson number near 1 is inconsistent with turbulence associated with Kelvin-Helmoltz instability but can be present at fronts that are symmetrically unstable. For such fronts, the boundary layers are not horizontally homogeneous and for steady geostrophic flows can be unstable for Richardson numbers greater than 0.25 since vertical particle motions can avoid KE loss to mixing by moving slantwise along sloping isopycnals (Thomas and Taylor 2010; D'Asaro et al. 2011). Here, the time dependent forcing and rapid boundary layer deepening near yearday 65.4, allows us to extend these concepts of SI-turbulence to the unsteady regime.

a. Ageostrophic shear and inertial motions in the boundary layer

Figures 2 and 3 reveal significant modulations of the flow and stratification in the boundary layer. Fig. 4 explores this variability more quantitatively using section averages, denoted by $\overline{(\cdot)}^{yz}$, of the shear and stratification, where the averages are conducted over the top 60 m and laterally across the extent of the front (defined by the 25.5 and 26.0 kg m^{-3} isopycnal surfaces). The vertical shear in the downstream direction (Fig. 4b), $\overline{\partial u/\partial z}^{yz}$ (blue circles), is compared to the geostrophic shear (black dashed line)

$$\frac{\partial u_g}{\partial z} = -\frac{1}{f}\frac{\partial b}{\partial y}, \tag{1}$$

where f is the Coriolis parameter. Similarly, Fig. 4c shows the section-averaged stratification $\overline{\partial b/\partial z}^{yz}$ (black stars). The vertical and lateral derivatives used in these and subsequent diagnostics were estimated using central differences.

Before yearday 65.2 the winds were weak and the section-averaged shear $\overline{\partial u/\partial z}^{yz}$ nearly equaled the geostrophic shear. As the storm moved through, however, $\overline{\partial u/\partial z}^{yz}$ first increased above the geostrophic shear, then decreased to nearly zero after yearday 65.5. Throughout the drift, the horizontal density gradient of the front remained relatively constant so that a strong geostrophic shear extended across the well-mixed boundary layer. As the winds slackened after yearday 66.5, the total shear, $\overline{\partial u/\partial z}^{yz}$, slowly increased, eventually overshooting the geostrophic shear.

Early in the record, the variations in shear had a similar time scale to inertial motions modified by the front's vertical vorticity, $\zeta = -\partial u/\partial y$. Such motions oscillate at the effective inertial frequency $f_{eff} = \sqrt{f(f+\zeta)}$ (e.g. Mooers 1975), which given the observed vorticity at the front, $\zeta \approx 0.6f$ (a value estimated from the cross-front averaged vorticity in the boundary layer, e.g. Fig. 2(a)-(e)), yields an effective inertial period $T_i = 2\pi/f_{eff} \approx 0.6$ days. Before yearday 65.6, the maximum and minimum in $\overline{\partial u/\partial z}^{yz}$ were separated by ~ 0.3 days, which is half of an effective inertial period. These observations are consistent with the hypothesis that variations in shear are the result of an inertial oscillation. Temporal oscillations of stratification provide further support for this hypothesis.

As schematized in Fig. 5, inertial shear at a front modifies the stratification through differential horizontal advection. By this mechanism, variations in stratification scale with the strength of the horizontal buoyancy gradient, M_o^2, and the amplitude of the inertial shear, $|\partial v_i/\partial z|$. If both of these quantities are constant, then the stratification in the boundary layer would follow the simple relation

$$N_i^2 = N_b^2 + \frac{M_o^2}{f_{eff}}\left|\frac{\partial v_i}{\partial z}\right|\cos\left(f_{eff}t + \varphi\right), \tag{2}$$

where N_b^2 is a constant background stratification in the boundary layer, and φ is a phase that makes the maxima in N_i^2 coincide with the maxima in the downstream component of the inertial shear, as dictated by the polarization relations. Using parameters representative of the observations, $N_b^2 = 1.5 \times 10^{-5}$ s^{-2}, $M_o^2 = 5 \times 10^{-7}$ s^{-2}, and $|\partial v_i/\partial z| = 0.003$ s^{-1}, we find that the simple physics encapsulated in (2) potentially explains the observed increases and subsequent decreases in shear and stratification through yearday 65.5, a hypothesis that we will explore more fully with the LES.

Beyond this time the inertial model predicts additional increases in both shear and stratification; instead, however, the boundary layer remains well mixed in density and momentum (Fig. 2, 4(*b*)-(*c*)). Potential vorticity and turbulence signatures, described in the next two sections, indicate that intense turbulence due to SI likely mixes the vertical shear thereby quelling the sheared inertial oscillations.

b. Evidence of a symmetrically unstable flow

The signature of a symmetrically unstable current is a geostrophic flow with potential vorticity (PV) of the opposite sign of the Coriolis parameter, absolute vorticity $(f+\zeta)$ of the same sign of the Coriolis parameter, and stable stratification (Thomas et al. 2013). All these conditions were met in the Gulf Stream during these measurements. Vertical vorticity and PV were computed assuming that the flow was hydrostatic and two-dimensional, i.e. that it did not vary in the downstream direction. Scaling arguments that justify this assumption are described in appendix A. Under these approximations $\zeta = -\partial u/\partial y$ and the PV is

$$q = \underbrace{(f+\zeta)N^2}_{q_{vert}} + \underbrace{\frac{\partial u}{\partial z}\frac{\partial b}{\partial y}}_{q_{bc}}. \tag{3}$$

Expressing the PV as a sum of two constituents emphasizes the contrasting roles of vertical vorticity/stratification and baroclinicity (encompassed in the terms labeled q_{vert} and q_{bc}, respectively). If the flow is geostrophic, (3) can be simplified to:

$$q_g = (f+\zeta)N^2 - f\left(\frac{\partial u_g}{\partial z}\right)^2 = fN^2\left[\left(1+\frac{\zeta}{f}\right) - \frac{1}{Ri_B}\right], \tag{4}$$

where the subscript "g" specifies that q_g is associated with the geostrophic flow, with Richardson number $Ri_B = N^2/(\partial u_g/\partial z)^2$. Written in this form, (4) implies that a geostrophic flow is symmetrically unstable when its Richardson number drops below the critical value, $Ri_c = (1+\zeta/f)^{-1}$.

This value is typically greater than the threshold for Kelvin-Helmholtz instability (0.25), even for strong currents with cyclonic vorticity like the Gulf Stream (Stone 1966).

Fig. 6 shows cross-stream sections of q_g, q and density. The geostrophic PV in the boundary layer grew progressively more negative through the period of strong mixing (Fig. 6(a)-(d)). The vertical vorticity averaged over the top 60 m was mostly cyclonic with the absolute vorticity $(f+\zeta)$ always positive (Fig. 2(a)-(e)). The combination of stable to marginal stratification, positive absolute vorticity, and negative q_g indicates that the geostrophic flow in the boundary layer was symmetrically unstable during the measurement period.

The total PV q is similar to q_g at the start of the drift but diverges over time (Fig. 6(f)-(j)) being more negative at yearday 65.35, just before the mixing event, but less negative at 65.61, just after the mixing event. The difference is due to the ageostrophic shear, which increases the total shear before the mixing event and decrease it afterwards (e.g. Fig. 4(b)). This is further evident in time series of the PV's constituents $\overline{q_{vert}}^{yz}$ and $\overline{q_{bc}}^{yz}$ plotted in Fig. 7b in blue and red, respectively. The two constituents exhibit much larger swings in magnitude than the PV itself, $\overline{q}^{yz}$ (green stars), because their variations mirror one another. This behavior is consistent with differential horizontal advection of density by inertial shear at a front, as illustrated in Fig. 5. The schematic shows how changes in stratification and q_{vert} are perfectly compensated by modifications in q_{bc} associated with the downstream component of the inertial shear throughout an inertial cycle. This is simply a manifestation of PV conservation when purely advective processes are involved. However, the presence of negative PV in the boundary layer cannot be explained by conservative processes alone and is consistent with removal of PV from the ocean due to atmospheric forcing.

Atmospheric forcing can drive frictional forces, $\mathbf{F}$, and Lagrangian changes in buoyancy, $\mathscr{D} = Db/Dt$, that result in a flux of PV through the sea surface

$$J^z = (\nabla_h b \times \mathbf{F}) \cdot \hat{\mathbf{z}} - (f + \zeta)\mathscr{D}, \tag{5}$$

where $\hat{\mathbf{z}}$ is a unit vector in the vertical (Thomas et al. 2013). Buoyancy loss and/or downfront winds (i.e. winds with a component in the direction of the thermal wind shear) drive upward PV fluxes that reduce the PV in the boundary layer at a rate that scales as

$$\frac{Dq}{Dt} \sim -\frac{\partial J^z}{\partial z} \sim -\frac{f}{H^2}(\mathrm{EBF} + B_o), \tag{6}$$

where H is the depth of the boundary layer, B_o the air-sea buoyancy flux, and $\mathrm{EBF} = \mathbf{M}_e \cdot \nabla_h b$ is the Ekman buoyancy flux that quantifies changes in buoyancy caused by advection of density by the Ekman transport, $\mathbf{M}_e$ (Thomas 2005; Thomas and Taylor 2010). The EBF was estimated over the drift using the downstream component of the wind-stress, τ_x^w, and the near-surface, y-averaged cross-stream buoyancy gradient $\overline{\partial b_s/\partial y}^y$

$$\mathrm{EBF} = -\frac{\tau_x^w}{\rho_o f}\overline{\frac{\partial b_s}{\partial y}}^y. \tag{7}$$

Both the EBF and buoyancy flux were positive over most of the drift, indicating that the atmospheric forcing was in the sense to reduce the PV in the boundary layer (Fig. 7(a)). Between yearday 65-67 the ocean was cooled by the atmosphere, with an average heat and buoyancy loss of 580 W m^{-2} and 7.0×10^{-7} m^2 s^{-3}, respectively. During this same period, the EBF was on average positive with a mean value of 3.5×10^{-7} m^2 s^{-3}, however it experienced considerable temporal variability. For example, the EBF peaked at a value of 3.3×10^{-6} m^2 s^{-3} near yearday 65.3 after ramping up from zero over a period of hours. (Fig. 7(a)). These fluctuations in the EBF were caused primarily by changes in the wind not the front. Given the mean values of the EBF and air-sea buoyancy flux, and the observed mixed layer depth, the scaling (6) suggests that decreases in PV of order 1×10^{-9} s^{-3} in 0.5 days are to be expected. Changes in $\overline{q}^{yz}$ of this magnitude are observed before yearday 65.6, however, after this time the mean PV in the boundary layer gradually increases in spite of the destabilizing forcing (Fig. 7(b)). This suggests that the wind- and cooling-driven surface PV fluxes are compensated by entrainment of high PV water from the pycnocline (Fig. 6). In the next section we characterize the turbulent processes that could have contributed to such entrainment.

c. Characteristics of the boundary layer turbulence

The vertical motion of the Lagrangian float measured the vertical velocity of the water and thus quantified the turbulent intensity in the boundary layer. The float repeatedly cycled across the boundary layer, carried by the larger turbulent eddies (Fig. 3ab). The envelope of the float track defines the layer of active mixing; the simplest measure of this depth H is twice the average float depth (Fig. 8b). The depth-average dissipation $\overline{\varepsilon}$ in the boundary layer can be estimated from the frequency spectra of float vertical acceleration using an inertial subrange method (Lien et al. 1998). Since the frequency spectra have a nearly universal shape, a second estimate is formed from the mean square vertical velocity $\langle w^2 \rangle$

$$\overline{\varepsilon_w} = 5.1 \langle w^2 \rangle^{1.5} / H, \tag{8}$$

where the constant has been chosen using a large set of high quality float data from Ocean Weather Station Papa (D'Asaro et al. 2014). Note that $\overline{\varepsilon_w}$ is really a measure of vertical kinetic energy, not dissipation; the two are dynamically related, but statistically nearly independent being dependent on different parts of the frequency spectrum. Fig. 8a plots the depth-integrated dissipations $\overline{\varepsilon}H$ (filled black circles) and $\overline{\varepsilon_w}H$ (open black circles). The maximum in $\overline{\varepsilon}H$ leads that of $\overline{\varepsilon_w}H$ slightly; this could easily be a sampling effect. Both, however, peak near yearday 65.4, the same time as the mixing event, confirming that the observed homogenization of shear and stratification coincides with a maximum in boundary layer turbulence.

We compare the observed dissipations with those expected from air-sea fluxes through the mechanisms that occur away from the front. In a convectively-driven boundary layer, the dissipation rate is approximately uniform with depth with a magnitude $\varepsilon_B = 0.6B_o$ (Shay and Gregg 1986). This makes a small contribution to the overall dissipation (Fig. 8a, green line). Estimating the wind and wave contributions is more difficult as the dynamics of this forcing is still not well understood (D'Asaro 2014). Traditionally, the dissipation in the interior of a wind- and wave-driven boundary layer scales with u_*^3, where the friction velocity $u_* = (\tau/\rho)^{0.5}$ depends on the wind stress τ and water density ρ. Higher values of dissipation, not sampled well by the float, are found in a wave-forced surface layer (Lombardo and Gregg 1989; Drennan et al. 1996) with dissipation rates decaying rapidly with depth. Furthermore, surface wave forcing through Stokes drift also does not scale exactly with u_*. We thus do not necessarily expect dissipation to scale as u_*^3. Instead, we generate an empirical prediction of the form $A\langle u_*\rangle^n$ and find optimal values for A and n using the dataset from D'Asaro et al. (2014). These data have similar winds as at the data here, but have little influence from fronts. Dissipation is computed using the same float-based methods. Fig. 9 shows the results using the parameterization

$$\overline{\varepsilon_w} H = 0.46\langle u_*\rangle^{2.4} \tag{9}$$

This yields an estimate of the depth-integrated dissipation rate due to wind/wave forcing (Fig. 8a, blue line). The buoyancy and wind forcing are summed to get the overall effect of air-sea forcing (red line). Although the proper way to combine these two effects is not well known, the uncertainty introduced by this is small since the buoyancy contribution is small. The sum roughly matches the overall shape of the dissipation curve, but on average falls below the measured values by about two standard deviations of the accuracy of (9). This suggests that additional forcing of the boundary layer may be needed. Simulations of steady wind-driven SI predict a boundary-layer-average dissipation associated with SI turbulence of half the Ekman buoyancy flux (Thomas and Taylor 2010). Data similar to that shown here (D'Asaro et al. 2011) suggests that this mechanism explains excess dissipation observed in the Kuroshio front. The pattern of EBF (Fig. 8a, cyan line) is similar to that of the wind forcing, but with a smaller magnitude. The sum of wind, buoyancy and EBF forcing (Fig. 8a, magenta dots) matches the measurements within the estimated errors for most of the data, suggesting that here, as in the Kuroshio data, SI could explain the excess dissipation. This is tempered by the uncertainty in how to combine the three contributions. During the dissipation peak near yearday 65.4, the measured dissipation is clearly larger than that predicted by air-sea fluxes alone and also larger than than predicted by air-sea fluxes and EBF. This additionally suggests that the unsteady aspects of SI could be important near the peak.

Thus, a semi-empirical comparison of the observed dissipation with that expected from air-sea forcing alone and that expected from SI, suggests that steady SI makes a significant (30-50%) contribution away from the mixing event. Additional dissipation at the mixing event could be due to unsteady SI. We investigate these hypotheses further using an LES of a symmetrically unstable flow in unsteady conditions, as described in the next section.

4. Large eddy simulation

a. Model description

In order to examine how inertial oscillations might modify symmetric instability in the Gulf Stream, we conducted a series of large-eddy simulations. The numerical method and setup of these simulations is very similar to simulations that have been previously used to study symmetric instability in the Gulf Stream (Thomas et al. 2013). In particular, the code is fully non-hydrostatic, uses a modified constant Smagorinsky scheme to model the subgrid-scale fluxes, second order finite differences in the vertical direction, a pseudo-spectral method in both horizontal directions, and a third order accurate mixed implicit/explicit Crank-Nicolson/Runge-Kutta timestepping algorithm. For details of the numerical method, see Taylor (2008).

The LES model is run in a 'frontal zone' configuration with a prescribed background horizontal buoyancy gradient used previously in similar studies, e.g. Thomas et al. (2013); Taylor and Ferrari (2010). The departure from this background density, and all other quantities are periodic in both horizontal directions. The simulation parameters are given in Table 1. The computational domain size is 1km in the cross-front direction, 500m in the along-front direction, and 120m in the vertical, and a sponge damping region is placed in the bottom 10m of the computational domain to prevent spurious reflections of downward-propagating internal gravity waves.

The model is initialized with a stable density profile chosen to approximate observed conditions. The buoyancy profile is set so that the Richardson number of the geostrophic flow, Ri_B, is a piecewise linear function increasing with depth. In particular, from $0 < z < -80$m Ri_B increases linearly from 0 at the surface to 1.5 at -80m depth. From $-80 < z < -120$m Ri_B increases linearly again from 1.5 to 5, and $Ri_B = 5$ for $z < -120$m. Note that since the mean vertical component of the relative vorticity is zero in the simulations due to the periodic boundary conditions, a portion of the upper layer is unstable to symmetric instability with $Ri_B < 1$. However, the LES does not capture a number of other physical processes that are likely to be important at the observational site. The along-front domain size is too small to permit baroclinic instability; there is no horizontal shear associated with the initial flow; and the influence of surface gravity waves is not included. Therefore, although the LES allows us to examine the influence of high frequency forcing and inertial oscillations on developing symmetric instability, it excludes baroclinic and barotropic instabilities and Langmuir turbulence.

b. Comparison to observations

In order to compare more directly with the observations, two simulations (with and without a front) have been run forced with the observed surface wind stress and buoyancy flux (see Figures 4a and 7a). The first simulation includes a background buoyancy gradient with $M^2 \equiv -\partial b/\partial y = 5 \times 10^{-7}\mathrm{s}^{-2}$, while the second does not ($M^2 = 0$). By comparing the two simulations, we can directly diagnose the influence of the front on the dynamical response. Both simulations are initialized at yearday 64.5 which was during a period of relatively weak forcing. This gives the simulations time to spin up before the strong storm that arrived at yearday 65.

Figure 10 shows time series of the stratification and shear averaged across the horizontal extent of the domain and from $-60\mathrm{m} < z < -5\mathrm{m}$. The upper 5m was excluded from the average to compare more directly with observations, and to exclude a thin boundary layer that forms in the simulations in response to the subgrid-scale LES viscosity. For comparison, the observed mean stratification and shear are also shown.

The agreement between the simulation with $M^2 = 5 \times 10^{-7}\mathrm{s}^{-2}$ and the observations is remarkable, particularly considering that aside from prescribing the initial density profile and forcing, the model is not tuned in any way to match the observations. A number of key features are accurately reproduced in the simulation. The shear and stratification both increase dramatically at yearday 65.25 in response to the strong wind forcing. By yearday 65.5, the stratification and shear are almost entirely eliminated in the upper 50m. Then, the stratification and shear gradually return over the course of about a day. Notably, the simulation without a background front does not exhibit this re-stratification and increase in shear, suggesting that frontal dynamics are responsible for the re-stratification. We will now analyze the model output in more detail to quantify the roles of inertial motions and symmetric instability in modulating the stratification and energetics of the turbulence in the boundary layer.

c. Wind-driven inertial motions in the boundary layer

The ageostrophic flow averaged laterally across the frontal zone has clear signatures of inertial motions (Fig. 11); namely, the two components of the flow oscillate nearly in quadrature and have a period close to $2\pi/f = 0.78$ days[2]. To determine if this is the case, we solved the equations governing the dynamics of wind-forced inertial motions averaged over the boundary layer depth H

$$\frac{dU_i}{dt} - fV_i = \frac{\tau_x^w}{\rho_o H} \tag{10}$$

$$\frac{dV_i}{dt} + fU_i = \frac{\tau_y^w}{\rho_o H}. \tag{11}$$

Solutions to (10) and (11) forced by the observed winds are compared to the ageostrophic flow from the LES in Fig. 11. We used a value of $H = 90$ m and an initial condition of $U_i = V_i = 0$ at yearday 64.5 for the calculation. The good agreement in amplitude and phasing between this simple model and the LES suggests that the oscillations are wind-forced inertial motions. However, the model cannot capture the vertical variations of the inertial motions, which are pronounced especially earlier in the record and can affect the stratification in the boundary layer as described in section 3a and schematized in Fig. 5.

[2]Note that because there is no mean vertical vorticity in the LES, inertial motions oscillate at $f_{eff} = f$

d. Stratification budget

To quantify the contribution of frontal dynamics and inertial motions to changes in stratification, terms in the laterally and vertically averaged stratification budget:

$$\frac{\partial \overline{N^2}^{xyz}}{\partial t} = \underbrace{\overline{\frac{\partial v}{\partial z}}^{xyz} M^2}_{\text{DHADV}} \underbrace{- \overline{\frac{\partial^2 w'b'}{\partial z^2}}^{xyz}}_{\text{N2MIX}} + \text{res} \tag{12}$$

were diagnosed in the simulation with $M^2 \neq 0$ and are illustrated in Figure 12. As with a typical mixed layer, differential mixing of buoyancy (N2MIX) is important. However, the rate of change in stratification follows more closely the differential horizontal advection of buoyancy (DHADV) indicating that the lateral density gradient of the front and inertial shear play an essential role in the re- and destratification of the boundary layer in contrast to a standard mixed layer model. Lateral advection generally contributes to an increase in stratification, with one important exception. Just prior to the minimum in stratification near yearday 65.5, DHADV reduces the stratification at a rate greater than N2MIX indicating that mixing alone cannot explain the destratification of the boundary layer at that time. In terms of the PV and its constituents, q_{vert} and q_{bc} (e.g. (3)), the reduction of the stratification and q_{vert} by DHADV at this time must be compensated by an increase in q_{bc} associated with inertial shear. Indeed, as illustrated in Fig. 11, near yearday 65.5 the inertial shear in the down-stream direction is negative, which opposes the thermal wind shear and increases q_{bc}.

e. Energetics of boundary layer turbulence

As in the observations, the storm that occurred during yearday 65 generated intense turbulence in the LES. Figure 13 shows a timeseries of the kinetic energy dissipation rate, ε, diagnosed from the LES (solid blue line). For comparison, the average dissipation rate estimated from the vertical acceleration of the Lagrangian float is shown in blue circles, along with the 95% confidence intervals. During the storm peak, the LES dissipation rate agrees very well with the observations. Following the peak storm, from yearday 65.6-67, the LES dissipation rate is consistently smaller than the observations. Note that the LES neglects a number of physical processes, notably surface wave breaking and Langmuir turbulence which might contribute additional dissipation. Nevertheless, we can use the LES results to diagnose the sources and sinks of turbulent KE.

SI-turbulence derives its KE from the so-called geostrophic shear production

$$GSP = -\overline{u'w'}^{xy}\,\overline{\frac{\partial u_g}{\partial z}}^{xy} \tag{13}$$

(primes denote deviations from the cross-front average), that quantifies the rate at which the turbulence removes kinetic energy from the balanced circulation (Taylor and Ferrari 2010; Thomas and Taylor 2010; Thomas et al. 2013). This distinguishes SI from convection which derives its KE from the release of potential energy via the turbulent buoyancy flux

$$BFLUX = \overline{w'b'}^{xy}. \tag{14}$$

Lastly, ageostrophic shear associated with wind-driven inertial motions or other flows could energize the turbulence through ageostrophic shear production

$$AGSP = -\overline{u'w'}^{xy}\left(\overline{\frac{\partial u}{\partial z}}^{xy} - \overline{\frac{\partial u_g}{\partial z}}^{xy}\right) - \overline{v'w'}^{xy}\,\overline{\frac{\partial v}{\partial z}}^{xy} \tag{15}$$

Time series of these three sources of turbulent kinetic energy (TKE) averaged over the boundary layer are shown in Figure 13. The Ekman buoyancy flux and imposed surface buoyancy flux are also shown for reference (dot-dashed). During the early stages of the storm, from yearday 65.2-65.5, the ageostrophic shear production (AGSP) is extremely large and dominates the production. During this period, the dissipation largely follows the AGSP. This time period coincides with the initial destratification of the boundary layer with a negative buoyancy flux (BFLUX) indicating transfer of kinetic to potential energy (mixing). During the latter half of yearday 65 when the boundary layer is destratified via DHAV by the action of inertial shear, the AGSP switches sign, and the GSP takes over as the dominant source of turbulent kinetic energy. During this period the GSP closely balances the dissipation, consistent with the energetics of SI.

The depth-averaged ageostrophic shear production (AGSP) and buoyancy flux (BFLUX) in the simulation with $M^2 = 0$ are also shown in Figure 13 for comparison. It is evident that in addition to providing a new source of TKE production through the GSP, the front also significantly modifies the AGSP and BFLUX. In the simulation with a front ($M^2 = 5 \times 10^{-7} \mathrm{s}^{-2}$), the maximum AGSP near yearday 65.3 is significantly enhanced relative to the simulation without a front. The development of stratification at the front concentrates the wind-driven shear in a relatively thin layer in the early stages of the storm, which appears to enhance the mean AGSP. Without the development of near-surface stratification, the simulation without a front also does not exhibit strong mixing (negative BFLUX) near yearday 65.3. In the later stages of the storm, following yearday 65.5, the AGSP remains positive in the simulation without a front, while it becomes a net sink of TKE in the simulation with a front. This highlights the qualitative change in the dominant energy pathways caused by the presence of a front as diagnosed from the LES. It should be noted, however, that near the peak of the storm the values of dissipation from the LES with and without a front are both consistent with the observed dissipation within the error bars of the estimate. Comparing this result to the findings illustrated in Figure 10 suggests that while frontal dynamics is of secondary importance to the overall energy budget of the turbulence, it is critical to the evolution of the mean stratification and shear.

The peak in GSP near yearday 65.5 in the LES does not correspond with a maximum in the EBF. This behavior is inconsistent with the parameterization for the energetics of SI under *steady* forcing proposed by Thomas et al. (2013). The parameterization builds off of the theoretical scaling of

Taylor and Ferrari (2010) that the sum of the GSP and BFLUX is a linear function of depth:

$$GSP + BFLUX \approx (EBF + B_o)\left(\frac{z+H}{H}\right), \tag{16}$$

where H is the depth of the layer with zero or negative PV. It then assumes that the buoyancy flux is a linear function of depth inside the so-called 'convective layer' of thickness h, defined by Taylor and Ferrari (2010), and zero below,

$$\text{BFLUX} \approx \begin{cases} B_o(z+h)/h & z > -h \\ 0 & z < -h \end{cases}. \tag{17}$$

Using (16), the GSP can thus be parameterized as

$$\text{GSP} \approx \begin{cases} (\text{EBF} + B_o)\left(\frac{z+H}{H}\right) - B_o\left(\frac{z+h}{h}\right) & z > -h \\ (\text{EBF} + B_o)\left(\frac{z+H}{H}\right) & -H < z < -h \\ 0 & z < -H \end{cases}. \tag{18}$$

While (18) does not hold instantaneously, it may be valid in a time-averaged sense. Eq. (16), which forms the basis of the parameterization, was derived based on a steady, turbulent Ekman balance, where accelerations are neglected. If the dominant acceleration is due to inertial motions, and if the time averaging window is longer than the inertial period, then the mean acceleration could be small, even if it is large instantaneously. If so, (18) could be skillful at predicting the time-mean GSP. To test this, the terms in the TKE equation were diagnosed from the LES, averaged in time, and compared to the predictions (16)-(18). However, to do so requires an estimate for the convective layer depth, h.

Taylor and Ferrari (2010) derived a scaling for h. They found that for *steady* forcing, turbulence driven by convection and down-front winds maintained a well-mixed layer for $z > -h$. When h was shallower than the layer with zero or negative PV (of thickness H), SI formed in the region $-h < z < -H$. Although the scaling derived in Taylor and Ferrari (2010) was for steady forcing, it is insightful to apply the scaling using the *instantaneous* surface wind and buoyancy flux. Here, H was diagnosed as the deepest location where $Ri_B < 2.5$.

The upper panel in Figure 14 shows the time evolution of the horizontally-averaged squared buoyancy frequency (N^2) from the LES with a front. This panel can be compared with the observed N^2 timeseries in Figure 3b, which shows many similar features. Notably, a region with very low stratification develops after the storm, starting from about 65.5, extending to a depth of approximately 75m. The stratification then re-develops, starting at depth near the start of yearday 66 with the stable region extending increasingly higher in the water column. The weakly stratified region coincides with low geostrophic Richardson number (Figure 14, middle panel). Starting from about yearday 66.5, most of the boundary layer has developed a stable stratification with $Ri_B \simeq 1$, indicating a neutral state with respect to symmetric instability.

Taylor and Ferrari (2010) defined the convective layer as the region with a positive buoyancy flux, $\langle w'b' \rangle > 0$. The horizontally-averaged buoyancy flux from the LES is shown in the bottom panel of Figure 14. White lines in Figure 14 show the predicted convective layer depth calculated from the instantaneous forcing strength using the scaling relation derived in Taylor and Ferrari (2010). The predicted convective layer depth captures the regions with positive buoyancy flux reasonably well, with the notable exception of the period between yearday 65.3 and 65.5 when the buoyancy flux was negative, indicating significant mixing. The convective layer depth also captures most of the regions with unstable stratification $N^2 < 0$ shown in purple in the top panel of Figure 14.

The time-averaged EBF, and air-sea buoyancy flux were used to predict the time-averaged convective layer depth and construct the parameterizations (17)-(18) which were compared to the time-mean GSP and BFLUX diagnosed from the LES (Figure 15). The average covered three inertial periods starting at yearday 65. The buoyancy flux is positive in the upper 20m, indicating that potential energy is converted to kinetic energy (i.e. convection) on average over these depths. The GSP is the dominant source of TKE, indicating that the thermal wind shear associated with the Gulf Stream provides most of the turbulent kinetic energy and, in turn, dissipation. The parameterizations (16)-(18) (dashed lines in the figure) match the LES results remarkably well, suggesting that they provide a skillful prediction for the time-averaged energy exchange terms associated with SI even when the surface forcing is strongly time-dependent.

5. Transient energetics of symmetric instability in the presence of inertial shear

While the time-averaged energetics of SI under variable winds can be described by the theoretical scalings for steady forcing, the transient energetics of SI deviate significantly from the predictions. This is particularly evident near yearday 65.5 when the GSP in the LES reached its maximum value while the EBF dropped to a minimum (e.g. Fig.13). Consistent with this discrepancy, around this time the float-based dissipation estimates exceeded the prediction of the theoretical scalings (Fig. 8). In this section we explore how inertial shear in a symmetrically unstable front can influence the energetics of SI and potentially explain this discrepancy. To this end we performed a linear stability analysis on a basic state that captures the key features of the Gulf Stream front, i.e. a flow with negative PV, stable stratification, and inertial shear.

a. Basic state

A simple configuration is used to study the effects of inertial motions on symmetric instability. It consists of an unbounded domain with a background velocity field

$$\overline{u} = \frac{M^2}{f} z\left[1+\gamma\cos(f_{eff}t-\phi)\right] - \zeta_g y \tag{19}$$

$$\overline{v} = -\gamma\left(\frac{M^2}{f_{eff}}\right) z\sin(f_{eff}t-\phi), \tag{20}$$

and buoyancy and pressure fields of the form

$$\overline{b} = N^2(t)z - M^2 y, \quad \overline{p} = -\rho_o \left[M^2 yz - \frac{1}{2} f \zeta_g y^2 - \frac{1}{2} N^2 z^2 \right], \tag{21}$$

where

$$N^2 = N_o^2 - \gamma \frac{M^4}{f_{eff}^2} \left[\cos\phi - \cos(f_{eff} t - \phi) \right], \tag{22}$$

and $N_o^2, M^2, \zeta_g, f_{eff} = \sqrt{f(f+\zeta_g)}, \gamma$, and ϕ are constants.

This basic state is an exact solution of the Boussinesq, inviscid, adiabatic equations of motion and represents a superposition of an inertial oscillation and a geostrophic flow with both vertical and lateral shears. The vertical shear of the inertial oscillation in the down-front (i.e. x) direction is assumed to scale with the thermal wind shear, differing by a factor of γ. The lateral shear and hence vertical vorticity, ζ_g, of the geostrophic flow modifies the frequency of the inertial oscillation, shifting it from f to f_{eff}. Changes in stratification are caused by the cross-front shear of the inertial oscillation which differentially advects buoyancy, as illustrated in Fig. 5. While the stratification, shear, and Richardson number change with time, the Ertel PV remains constant and equal to

$$\overline{q} = (f + \zeta_g) N^2 + \frac{\partial \overline{u}}{\partial z} \frac{\partial \overline{b}}{\partial y} = \frac{f_{eff}^2}{f} N_o^2 - \frac{M^4}{f} (1 + \gamma \cos\phi) \tag{23}$$

as required by PV conservation. It is important to note that at a front, the presence of an inertial oscillation can affect the value of the PV. The reason for this is that the horizontal component of the vorticity associated with the oscillation can project into the horizontal buoyancy gradient of the front. How large of a contribution this is depends on both the strength of the inertial shear (i.e. γ) and the phase of the oscillation ϕ. If at $t = 0$ the inertial shear is entirely in the down-front direction (i.e. $\phi = 0$) then the PV is reduced relative to the case with no inertial oscillation since the inertial and thermal wind shears add. When the inertial shear is entirely cross-front at $t = 0$, i.e. $\phi = \pi/2$, then the PV is unaffected by the oscillation. The fact that the PV depends on the properties of the inertial oscillation at the initial time might seem like a theoretical construct. However the contribution to the PV from the inertial oscillation can be interpreted physically as the PV anomaly generated by the impulsive, presumably wind-driven, frictional torque needed to accelerate the horizontal component of the vorticity of the inertial motion by $t = 0+$. With this interpretation, the phase ϕ is determined by the direction of the impulsive force relative to the front, e.g. if the force is downfront $\phi = 0$, while if it is upfront $\phi = \pi$.

b. Stability analysis

The basic state is perturbed with a 2D (i.e. invariant in the x-direction) disturbance, with velocity, buoyancy, and pressure fields $\mathbf{u}'(y,z,t)$, $b'(y,z,t)$, and $p'(y,z,t)$. The perturbation that we investigate is characterized by streamlines in the $y-z$ plane that run parallel to isopycnals and corresponds to the fastest growing mode for SI in a basic state with no inertial shear (i.e. $\gamma = 0$). The method of solving the evolution of the perturbations is described in appendix B. A basic state with parameters representative of the observations from the Gulf Stream, i.e. $\overline{q} = -5\times10^{-10}$ s^{-3}, $M^2 = 5\times10^{-7}$ s^{-2}, $f = 9.2\times10^{-5}$ s^{-1}, $\zeta_g = 0.6f$, and $\gamma = 0.67$ is used in the calculation.

A timeseries of the kinetic energy per unit mass, $KE = |\mathbf{u}'|^2/2$, of a perturbation added to this basic state is shown in Fig. 16(b). The KE of SI in a basic state without an inertial oscillation ($\gamma = 0$) yet with the same PV ($\overline{q} = -5\times10^{-10}$ s^{-3}) and geostrophic shear ($M^2 = 5\times10^{-7}$ s^{-2}) but lower stratification ($N_o^2 = 1.5\times10^{-5}$ s^{-2}) is also shown in the figure for comparison and exhibits exponential growth. Comparing the evolution of the KE for the two basic states reveals that SI in an inertial oscillation experiences periods of explosive growth. These occur at times when the stratification approaches its minimum (e.g. near $t = 0.3$ and 0.9 days), resulting in a forty-fold increase in KE in a tenth of a day. If the perturbation were allowed to develop secondary instabilities and turbulence, then presumably the period of explosive growth would correspond to a peak in turbulent dissipation. With these considerations in mind, we can interpret the timing of the maximum excess dissipation near yearday 65.5 seen in the observations (Fig. 8(a)) as being caused by a rapid growth of SI during the weakening stratification at this time (Fig. 4(c)).

Analysis of the perturbation KE reveals the instability's source of energy. The analysis involves a KE budget, which is governed by the following equation

$$\frac{D}{Dt}KE = \underbrace{-u'w'\frac{M^2}{f}}_{GSP}\underbrace{-v'w'\frac{\partial \overline{v}}{\partial z} - u'w'\left(\frac{\partial \overline{u}}{\partial z} - \frac{M^2}{f}\right)}_{AGSP}\underbrace{-\nabla \cdot \mathbf{u}'p'}_{PWORK} + \underbrace{w'b'}_{BFLUX} . \tag{24}$$

derived by taking the dot product of $\mathbf{u}'$ with (B1). KE can be changed by convergences/divergences of the energy flux (PWORK) and the release of potential energy via the buoyancy flux (BFLUX). The disturbances can also exchange KE with the background flow through shear production. In fact, given that SI does not induce pressure and buoyancy anomalies, the only way to change its KE is through shear production. The shear production is further decomposed into its geostrophic and ageostrophic parts (GSP and AGSP respectively) with the latter representing the rate of KE extraction from the inertial oscillation.

During the period of explosive growth near 0.3 and 0.9 days, $GSP > 0$ while $AGSP < 0$, indicating that SI gains KE from the geostrophic flow while losing KE to the inertial oscillation (Fig. 16(c)). From this we can conclude that the enhanced growth is not associated with an extra energy source from the inertial shear. Instead, this difference in growth can be attributed to the temporal modulation of the stratification and GSP. In particular, the GSP intensifies as the stratification weakens. During these times isopycnals and hence perturbation streamlines steepen, leading to stronger vertical velocities and momentum fluxes and an amplification of the GSP. With this physics in mind, we interpret the maximum in GSP near yearday 65.5 seen in the LES (Fig. 13) as resulting from the interplay of inertial shear and the front which tilts isopycnals, reduces the stratification through differential horizontal advection, DHAV (Fig. 12), and leads to a more efficient extraction of KE from the geostrophic flow by SI.

6. Summary and discussion

Observations from the North Wall of the Gulf Stream made during the passage of a storm revealed a symmetrically unstable flow superposed with strongly sheared inertial motions. The event could be described in three phases, an initial phase where the stratification oscillated in time, a middle period where density and momentum in the boundary layer were well mixed, and a latter phase where the stratification and frontal vertical shear were restored to pre-storm values. Turbulent dissipation estimates from a Lagrangian float cycling in the boundary layer were elevated relative to the expected TKE production by wind and air-sea buoyancy fluxes, implying that the frontal currents were an additional source of energy that was being tapped by SI. During the oscillatory stratification phase, however, the observed excess dissipation was significantly larger than that predicted by theoretical scalings for the energetics of SI under steady conditions.

The observational findings were interpreted using an LES configured with forcing and frontal characteristics taken from the observations and a linear stability analysis of a symmetrically unstable flow interacting with inertial motions. The LES illustrates how differential horizontal advection of buoyancy by inertial shear generated the oscillations in stratification during the initial passage of the storm. A stability analysis shows that at the phase of the oscillation when the stratification approaches its minimum, SI experiences explosive growth, extracting KE from the frontal flow at an enhanced rate relative to SI in steady conditions. This result is played out in the LES and might explain the excess dissipation seen in the observations during the period of oscillatory stratification.

While the energetics of SI driven by variable winds and interacting with inertial motions is transient, averaged over several inertial periods it is well predicted by parameterizations based on theory developed for steady forcing. This suggests that these parameterizations could be used to estimate the global net sink of the ocean circulation's KE by SI using wind fields averaged over a few inertial periods. Starting on a smaller scale, we attempt to assess the importance of the process to the overall energetics of the Gulf Stream. The time-mean of the GSP averaged over the upper 50 m from the LES at the peak of the storm, i.e. between yearday 65.3-65.5, is $2.3 \times 10^{-6}\mathrm{m}^2/\mathrm{s}^3$ (Figure 13). We can compare this to the baroclinic kinetic energy associated with the thermal wind shear, i.e. $1/2[\int(M^2/f)dz]^2$. Based on the thermal wind associated with a lateral buoyancy gradient of $5 \times 10^{-7}\mathrm{s}^{-2}$, the baroclinic kinetic energy over the upper 50 m is $0.037\mathrm{m}^2/\mathrm{s}^2$. Without a source of energy to maintain the mean flow, the level of GSP during the peak of the storm would be able to entirely eliminate the thermal wind shear in less than 4.5 hours. This is close to the duration of the period of intensified GSP, suggesting that SI could explain the near homogenization of momentum in the boundary layer subsequent to the initial passage of the storm.

After the boundary layer was mixed, the thermal wind shear and stratification were restored to pre-storm values. The fact that the stratification remained relatively weak and the Richardson number near one suggests that submesoscale mixed-layer baroclinic instability (MLI) was not dominant during the drift (Boccaletti et al. 2007; Fox-Kemper et al. 2008). Indeed, the close correspondence between the observations and LES, which is not capable of simulating baroclinic instability, further supports this inference. It is not obvious why the front did not show clear signs of restratification by finite-amplitude MLI. However, it could simply be that the duration of the drift was not long enough for the effects of finite-amplitude MLI to be noticeable. For example, for $0 < Ri_B < 1$, the e-folding time corresponding to the growth rate of the fastest growing mode of ageostrophic baroclinic instability is between 12-17 hours (Stone 1970). Simulations of MLI at fronts with initial Richardson numbers in this range show that it takes several days, i.e. longer than the duration of the drift, for finite-amplitude MLI to increase the mixed layer stratification beyond what is attributable to SI (e.g. Fig. 3 of Fox-Kemper et al. 2008).

The temporal evolution of the stratification and shear towards the end of the drift is reminiscent of geostrophic adjustment at a front, a problem that has been studied theoretically, primarily in the inviscid, adiabatic limit (e.g. Ou 1984; Tandon and Garrett 1994; Shakespeare and Taylor 2013). In this limit, PV conservation and geostrophy constrain the value of the time-mean stratification and shear, and inertial motions drive oscillations about this mean. The observations indicate, however, that PV is not conserved and changes sign over time, e.g. Figures 7(b) and 8(c). Furthermore in the latter phase of the record, the down-stream shear asymptotes towards, rather than oscillates about, the thermal wind-balance, suggesting that any sheared inertial motions that were present were damped (Figure 10). These differences from the inviscid, adiabatic theory are likely attributable to SI which drives turbulence and entrains high PV water from the pycnocline into the boundary layer. A detailed study of geostrophic adjustment in a symmetrically unstable flow is beyond the scope of this work, but will be the subject of future research.

Acknowledgments. We are grateful to Jason Gobat, Eric Boget, Dave Winkel, Ben Jokinen, Mike Johnson, and the captains and crews of the *R/Vs Knorr* and *Atlantis* who made the collection of these observations in challenging wintertime conditions possible. This work was supported by ONR grants N00014-09-1-0202 under the Scalable Lateral Mixing and Coherent Turbulence Departmental Research Initiative. Additional support came from ONR grants N00014-09-1-0266 (C.M.L. and A.S.) and N00014-09-1-0172 (E.A.D. and A.S.).

APPENDIX A

In this appendix we estimate the magnitude of the terms involving downstream variability that we neglected in our computation of the PV (3). The terms that are missing from (3) in the hydrostatic limit are

$$q_{res} = \frac{\partial v}{\partial x} N^2 - \frac{\partial v}{\partial z}\frac{\partial b}{\partial x}$$

If the first term were important, then there would be a significant amount of variance in v associated with along-stream variations that would not be seen in the LES. In the top panel of Fig. 17 we compare histograms of v from the Knorr and Atlantis observations and the LES. The standard deviations of v in the Knorr observations and the LES results are the same, i.e. 0.12 m s^{-1}, while the standard deviation from the Atlantis observations is 0.17 m s^{-1}. This suggest that most of the variance in v is explained by inertial motions not balanced motions since the cross-stream velocity in the LES is dominated by the former. If the excess variance in the Atlantis observations, ~ 0.05 m s^{-1}, were associated with along-stream variations, and if the flow were isotropic $\partial/\partial x \sim \partial/\partial y \sim 1/(10km)$, then this would result in a vertical vorticity of $\partial v/\partial x \sim 1\times10^{-5}$ s^{-1} which is an order of magnitude smaller than the vertical vorticity associated with the down-stream component of the velocity, $-\partial u/\partial y$. This is likely an upper bound for $\partial v/\partial x$ since the flow at a front is far from isotropic, that is the characteristic length scale of the flow in the cross-stream direction is much smaller than that in the along-stream direction.

The second term in q_{res} involves a buoyancy gradient in the along stream direction, $\partial b/\partial x$. If there were such a gradient, then it would be associated with a thermal wind shear in the cross-stream direction, $\partial v_g/\partial z = (1/f)\partial b/\partial x$, which should be detectable in the observations of $\partial v/\partial z$. The histogram of $\partial v/\partial z$ from the Knorr observations is shown in the bottom panel of Fig. 17. The mean of the distribution is 0.0016 s^{-1}. If this mean value were attributed to a flow in thermal wind balance it would correspond to an along-stream buoyancy gradient of 1.5×10^{-7} s^{-2}, which is $\sim 1/3$ the strength of the cross-front buoyancy gradient. If so, the contribution to the PV from this thermal wind shear would be $-(1/f)(\partial b/\partial x)^2 \sim -1\times 10^{-10}$ s^{-3} which is an order of magnitude weaker than the PV anomaly associated with the cross-stream buoyancy gradient (e.g. $\overline{q_{bc}}^{yz}$ in Fig. 7b near the beginning of the record).

In summary we estimate that the terms in the PV and the vertical vorticity associated with along-front variability are an order of magnitude weaker than the terms that we retained in our 2D approximation and thus it is justifiable to neglect them.

APPENDIX B

The dynamics of the 2D perturbations $\mathbf{u}'(y,z,t)$, $b'(y,z,t)$, and $p'(y,z,t)$ are governed by the incompressible, Boussinesq equations:

$$\frac{D\mathbf{u}'}{Dt} + \mathbf{u}'\cdot\nabla\overline{\mathbf{u}} + \mathbf{u}'\cdot\nabla\mathbf{u}' + f\hat{\mathbf{z}}\times\mathbf{u}' = -\frac{1}{\rho_o}\nabla p' + b'\hat{\mathbf{z}} \quad \text{(B1)}$$

$$\frac{Db'}{Dt} + \mathbf{u}'\cdot\nabla\overline{b} + \mathbf{u}'\cdot\nabla b' = 0 \quad \text{(B2)}$$

$$\nabla\cdot\mathbf{u}' = 0, \quad \text{(B3)}$$

where $D/Dt = \partial/\partial t + \overline{v}\partial/\partial y$ is the rate of change following the background flow. Since the perturbations are 2D, the flow in the $y-z$ plane can be expressed in terms of a streamfunction, i.e. $v' = \partial\psi/\partial z$, $w' = -\partial\psi/\partial y$. Due to the lack of boundaries, and to the spatially-uniform gradients of the basic state, the method of Craik (1989) can be employed, i.e. solutions of the form of plane waves

$$\begin{bmatrix} u' \\ \psi \\ b' \\ p' \end{bmatrix} = \begin{bmatrix} U(t) \\ \Psi(t) \\ B(t) \\ P(t) \end{bmatrix} e^{\mathrm{i}\varphi} + \text{c.c.}, \tag{B4}$$

are sought, where $\varphi = ly + mz$ is the phase and $\mathbf{k} = (l, m)$ is the wavevector which is spatially uniform, yet varies with time. The evolution of only a single plane wave is considered, which makes the nonlinear terms in (B1)-(B2) identically equal to zero. With the ansatz (B4) it follows that the phase does not change following the background flow, i.e. $D\varphi/Dt = 0$, yielding the following solution for the wavevector:

$$l = l_o; \quad m = m_o + \gamma \frac{M^2}{f_{eff}^2} \left[\cos\phi - \cos(f_{eff}t - \phi)\right] l_o, \tag{B5}$$

where (l_o, m_o) denotes its initial value.

Substituting the ansatz (B4) into (B1)-(B3), and deriving a streamwise vorticity equation to eliminate pressure, yields a set of three coupled ODEs for the amplitude of the disturbance $\mathbf{a} = [U\ \Psi\ B]^T$:

$$\dot{\mathbf{a}} = \mathsf{E}(t)\mathbf{a}, \tag{B6}$$

where $\dot{()}$ denotes a time derivative and the matrix E has the elements:

$$\begin{array}{lll} \mathsf{E}_{11} = 0 & \mathsf{E}_{12} = \mathrm{i}\left(\frac{f_{eff}^2}{f}\right) m + \mathrm{i}\frac{M^2}{f}[1 + \gamma\cos(f_{eff}t - \phi)]l & \mathsf{E}_{13} = 0 \\ \mathsf{E}_{21} = \mathrm{i}mf|\mathbf{k}|^{-2} & \mathsf{E}_{22} = -(\dot{|\mathbf{k}|^2})|\mathbf{k}|^{-2} & \mathsf{E}_{23} = \mathrm{i}l|\mathbf{k}|^{-2} \\ \mathsf{E}_{31} = 0 & \mathsf{E}_{32} = \mathrm{i}\left(lN^2 + mM^2\right) & \mathsf{E}_{33} = 0 \end{array}$$

In the absence of an inertial oscillation ($\gamma = 0$), a geostrophic background flow of the form (19) is symmetrically unstable when $f\overline{q} < 0$. For these conditions, the fastest growing mode is characterized by streamlines that run parallel to isopycnals, with a wavevector $-l/m = M^2/N^2$

(Taylor and Ferrari 2009). The effects of inertial oscillations on the dynamics of this particular mode for $\gamma \neq 0$ can be explored by choosing initial components of the wavevector that satisfy the following relation

$$\frac{l_o}{m_o} = -\frac{M^2}{N_o^2}, \tag{B7}$$

which forces $-l/m = M^2/N^2$ for all times. With this initial condition it follows that $\mathsf{E}_{32} = 0$ and thus the buoyancy anomaly of the perturbation is zero, i.e. $B(t) = 0$. The evolution of the amplitude of the perturbation is governed by

$$[\dot{U}\ \dot{\Psi}]^T = \mathsf{F}[U\ \Psi]^T \tag{B8}$$

where the matrix F has elements $\mathsf{F}_{11} = \mathsf{E}_{11}$, $\mathsf{F}_{12} = \mathsf{E}_{12}$, $\mathsf{F}_{21} = \mathsf{E}_{21}$, and $\mathsf{F}_{22} = \mathsf{E}_{22}$, and was solved numerically.

References

Alford, M., 2003: Redistribution of energy available for ocean mixing by long-range propagation of internal waves. *Nature*, **423**, 159–163.

Boccaletti, G., R. Ferrari, and B. Fox-Kemper, 2007: Mixed layer instabilities and restratification. *J. Phys. Oceanogr.*, **37**, 2228–2250.

Craik, A. D. D., 1989: The stability of unbounded two- and three-dimensional flows subject to body forces: some exact solutions. *J. Fluid Mech.*, **198**, 275–292.

D'Asaro, E., 2003: Performance of autonomous lagrangian floats. *J. Atmos. Oceanic Technol.*, **20**, 896–911.

D'Asaro, E., C. M. Lee, L. Rainville, R. Harcourt, and L. N. Thomas, 2011: Enhanced mixing and energy dissipation at ocean fronts. *Science*, **15**, 318–322.

D'Asaro, E. A., 2014: Turbulence in the upper-ocean mixed layer. *Annual Review of Marine Science*, **6 (6)**.

D'Asaro, E. A., J. Thomson, A. Y. Shcherbina, R. R. Harcourt, M. F. Cronin, M. A. Hemer, and B. FoxKemper, 2014: Quantifying upper ocean turbulence driven by surface waves. *Geophysical Research Letters*, **41 (1)**, 102–107.

Drennan, W. M., M. A. Donelan, E. A. Terray, and K. B. Katsaros, 1996: Oceanic turbulence dissipation measurements in swade. *J. Phys. Oceanogr.*, **26**, 808–815.

Edson, J. B., and Coauthors, 2013: On the exchange of momentum over the open ocean. *J. Phys. Oceanogr.*, **43**, 43, 1589–1610.

Firing, E., and J. Hummon, 2010: Ship-mounted acoustic doppler current profilers. *The GO-SHIP Repeat Hydrography Manual: A Collection of Expert Reports and Guidelines*, E. Hood, C. Sabine, and B. Sloyan, Eds., iOCCP Report Number 14, ICPO Publication Series Number 134.

Fox-Kemper, B., R. Ferrari, and R. Hallberg, 2008: Parameterization of mixed layer eddies. Part I: Theory and diagnosis. *J. Phys. Oceanogr.*, **38**, 1145–1165.

Lien, R. C., E. A. D'Asaro, and G. Dairiki, 1998: Lagrangian frequency spectra of vertical velocity and vorticity in high-Reynolds-number oceanic turbulence. *J. Fluid Mech.*, **362**, 177–198.

Lombardo, C. P., and M. C. Gregg, 1989: Similarity scaling of viscous and thermal dissipation in a convecting surface boundary layer. *J. Geophys. Res.*, **94**, 6273–6284.

Lueck, R., and J. Picklo, 1990: Thermal inertia of conductivity cells: Observations with a Sea-Bird cell. *J. Atmos. Oceanic Technol.*, **7**, 756–768.

Marshall, J., and Coauthors, 2009: The climode field campaign: Observing the cycle of convection and restratification over the gulf stream. *bams*, **90**, 1337–1350.

Mooers, C. N. K., 1975: Several effects of a baroclinic current on the cross-stream propagation of inertial-internal waves. *Geophys. Fluid Dyn.*, **6**, 245–275.

Morison, J., R. Anderson, N. Larson, E. D'Asaro, and T. Boyd, 1994: The correction for thermal-lag effects in Sea-Bird CTD data. *J. Atmos. Oceanic Technol.*, **11**, 1151–1164.

Ou, H., 1984: Geostrophic adjustment: a mechanism for frontogenesis? *J. Phys. Oceanogr.*, **14**, 994–1000.

Shakespeare, C. J., and J. R. Taylor, 2013: A generalized mathematical model of geostrophic adjustment and frontogenesis: uniform potential vorticity. *J. Fluid Mech.*, **736**, 366–413.

Shay, T. J., and M. C. Gregg, 1986: Convectively driven turbulent mixing in the upper ocean. *J. Phys. Oceanogr.*, **16**, 1777–1798.

Stone, P., 1966: On non-geostrophic baroclinic stability. *J. Atmospheric Sciences*, **23**, 390–400.

Stone, P., 1970: On non-geostrophic baroclinic stability: Part II. *J. Atmospheric Sciences*, **27**, 721–726.

Tandon, A., and C. Garrett, 1994: Mixed layer restratification due to a horizontal density gradient. *J. Phys. Oceanogr.*, **24**, 1419–1424.

Taylor, J., 2008: Numerical simulations of the stratified oceanic bottom boundary layer. Ph.D. thesis, University of California, San Diego.

Taylor, J., and R. Ferrari, 2009: The role of secondary shear instabilities in the equilibration of symmetric instability. *J. Fluid Mech.*, **622**, 103–113.

Taylor, J., and R. Ferrari, 2010: Buoyancy and wind-driven convection at a mixed-layer density fronts. *J. Phys. Oceanogr.*, **40**, 1222–1242.

Thomas, L. N., 2005: Destruction of potential vorticity by winds. *J. Phys. Oceanogr.*, **35**, 2457–2466.

Thomas, L. N., and J. R. Taylor, 2010: Reduction of the usable wind-work on the general circulation by forced symmetric instability. *Geophys. Res. Lett.*, **37**, L18 606, doi:10.1029/2010GL044680.

Thomas, L. N., J. R. Taylor, R. Ferrari, and T. M. Joyce, 2013: Symmetric instability in the Gulf Stream. *Deep-Sea Res. II*, **91**, 96–110.

Wunsch, C., 1998: The work done by the wind on the oceanic general circulation. *J. Phys. Oceanogr.*, **28**, 2332–2340.

LIST OF TABLES

TABLE 1. Parameters for the large-eddy simulation

(LX, LY, LZ)	(NX, NY, NZ)	db/dy	f
(1000 m, 500 m, 120 m)	(256,128,64)	$\left(5\times10^{-7}\ \mathrm{s}^{-2}, 0\right)$	$9.3\times10^{-5}\ \mathrm{s}^{-1}$

LIST OF FIGURES

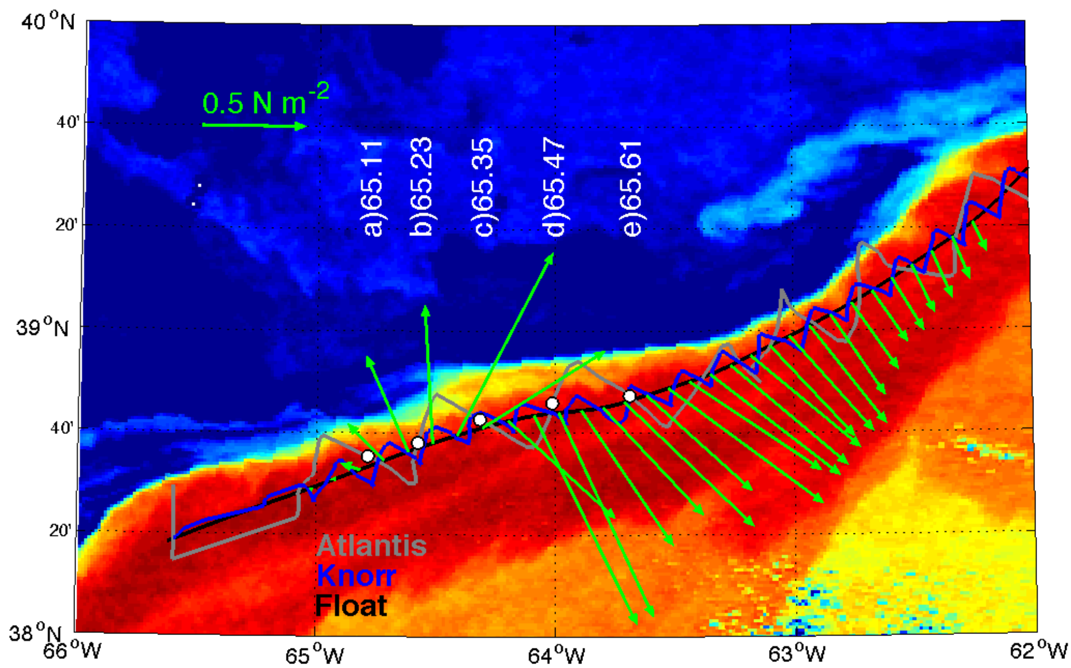

904 FIG. 1. The tracks of the *R/V Knorr* (blue) and the *R/V Atlantis* (gray), the path of the Lagrangian float (black), and the wind stress (green vectors) during part of the Lagrangian drift between March 5-9 (yearday 64-68) superimposed on an image of the sea surface temperature on March 12 illustrating the prominent front on the North Wall of the Gulf Stream where the experiment was conducted. Each wind stress vector originates at the location of the float at the time of the wind measurement. The times (in yeardays) when the sections shown in figures 2 and 6 were taken are indicated, and are located at the central longitude of each section.

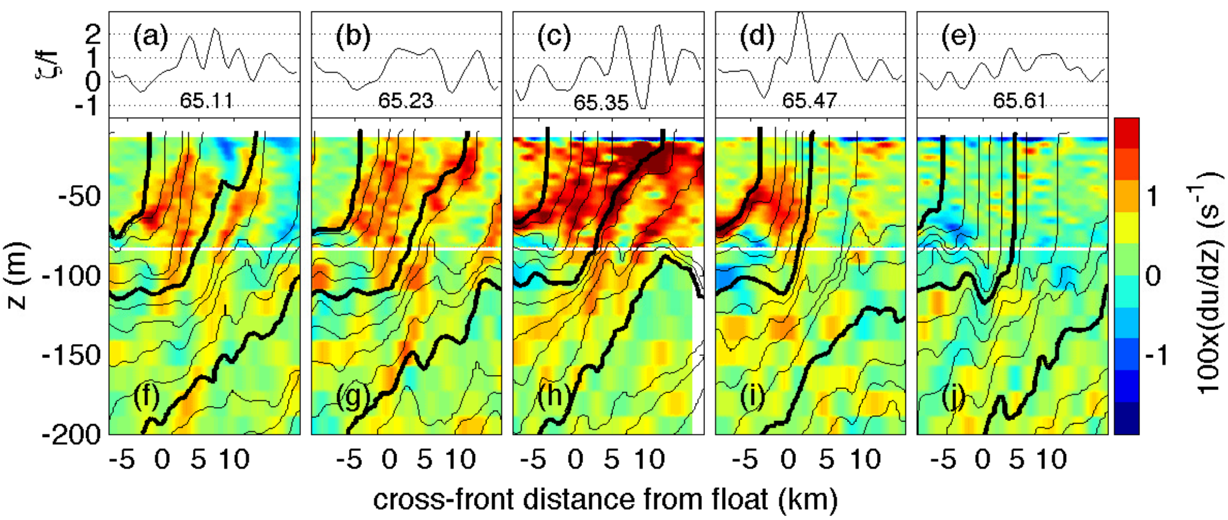

FIG. 2. Cross-stream structure of vertical and lateral shear at selected times from *Atlantis*. Top row (a)-(e): vertical vorticity averaged over the top 60 m normalized by f. Bottom row (f)-(j): Cross-stream sections of density (contours) and the downstream component of the vertical shear, $\partial u/\partial z$ (shades). Density is contoured every 0.1 kg m^{-3} and the thicker contours denote the 25.5, 26.0, and 26.5 kg m^{-3} isopycnal surfaces. The time when the sections were taken is indicated in yeardays in the upper panels.

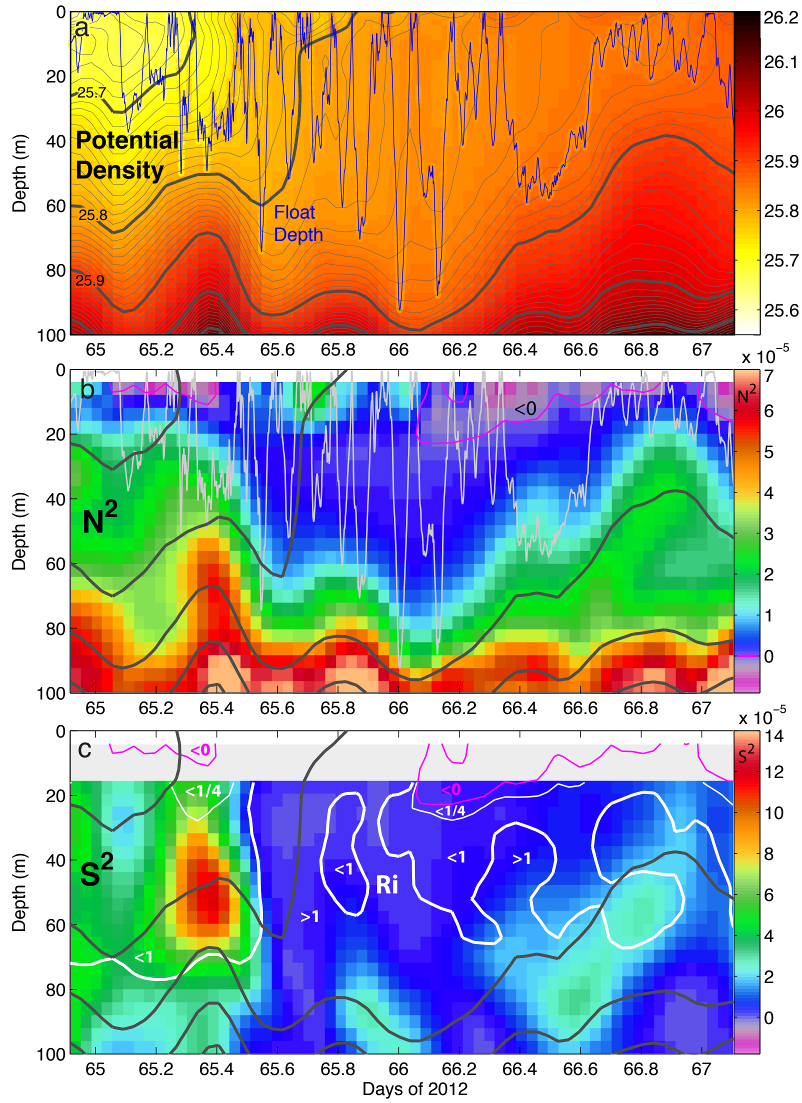

FIG. 3. Time series of stratification and shear from *Knorr* along the float trajectory. a) Potential density (colors) interpolated to a uniform grid from all Triaxus profiles within 3 km of the float and float depth (blue line) underlaid by density measured at the float colored on the same scale. The float density is nearly invisible showing that the mapped Triaxus data is not significantly aliased by space and time variability at the front. b) N^2, the squared buoyancy frequency (colors) computed from the mapped potential density, float depth (white) and selected potential density contours from panel a). Regions of unstable stratification are colored magenta-blue and demarcated by the thin magenta line. c) S^2, the mean squared total shear, computed from the mapped 75 kHz *Knorr* ADCP velocity components and selected potential density contours from panel a). White lines denote regimes of gradient Richardson number $Ri = N^2/S^2$ demarcating regions larger and smaller than 1 and 0.25. Magnenta lines demarcate regions with $Ri < 0$ as in panel b). Maps were made from all data within the domain averaged with a Guassian smoother of width 8 m in the vertical and 6000 seconds in time.

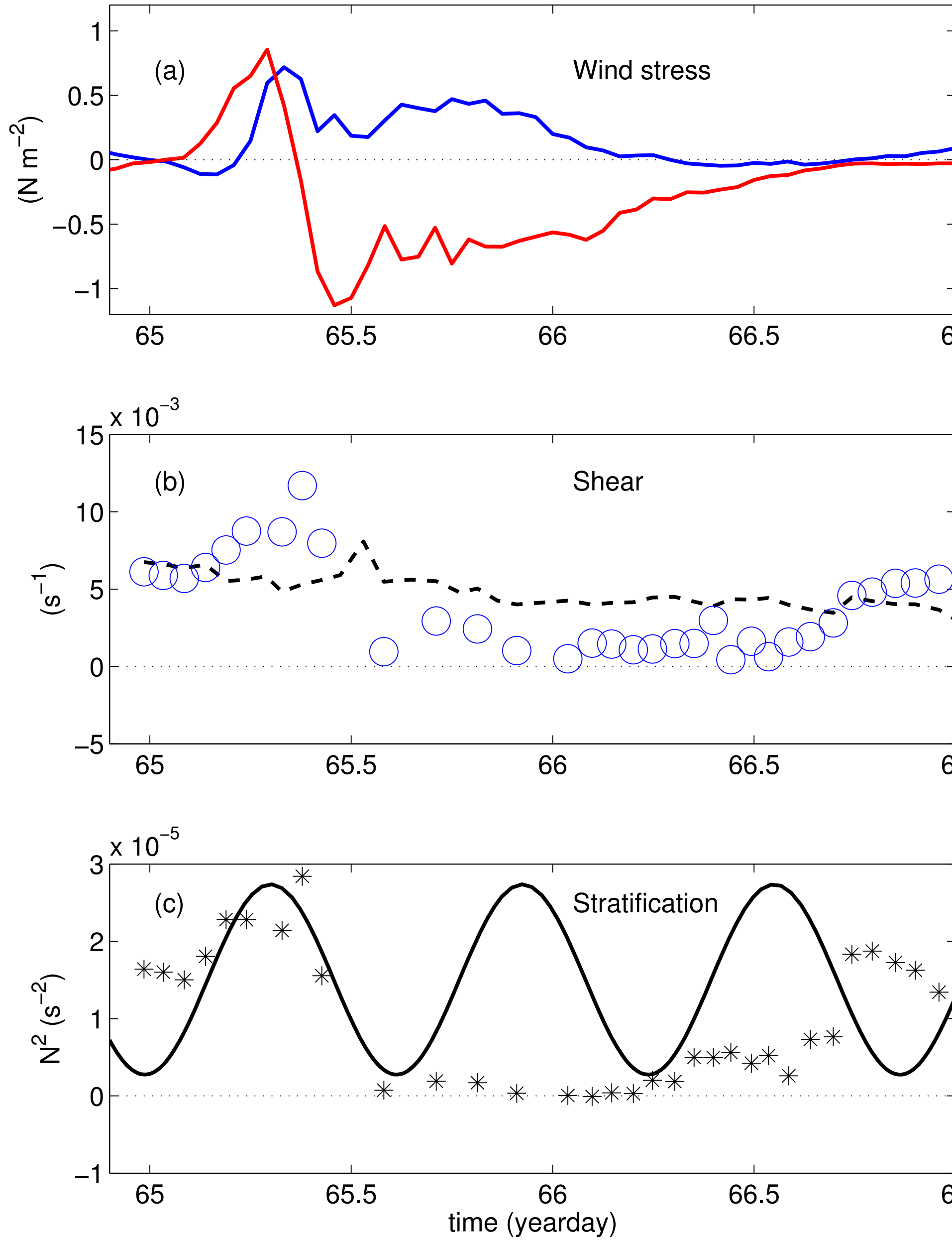

FIG. 4. a) Time series of the downstream (blue) and cross-stream (red) components of the wind stress. b) The section-averaged down-stream component of the vertical shear, $\overline{\partial u/\partial z}^{yz}$, (blue circles) and the geostrophic shear $\overline{\partial u_g/\partial z}^{yz}$ (dashed black). c). The section-averaged stratification in the boundary layer, $\overline{\partial b/\partial z}^{yz}$, (stars), and the oscillatory variations in stratification (black line) caused by inertial shear at a front, N_i^2, as predicted by (2). The phase in the model was chosen so that a maximum in N_i^2 aligned with the maximum in the observed downstream component of the vertical shear at about yearday 65.3.

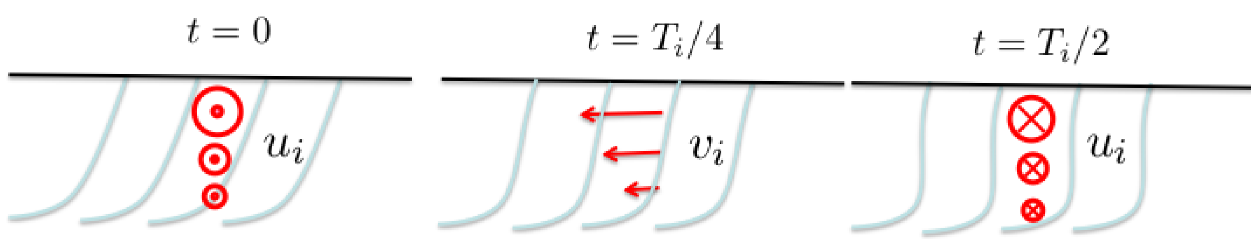

932 FIG. 5. Schematic illustrating how inertial shear at a front modifies the stratification in the boundary layer. A vertically-sheared inertial motion (u_i, v_i) (red) steepens isopycnals (blue lines) and reduces the stratification for times between the maximum and minimum in the downstream velocity (left and right panels, respectively). The process is purely advective and hence PV remains constant throughout the inertial cycle. As a consequence, the stratification anomaly and down-stream component of the inertial shear, $\partial u_i / \partial z$, are in phase.

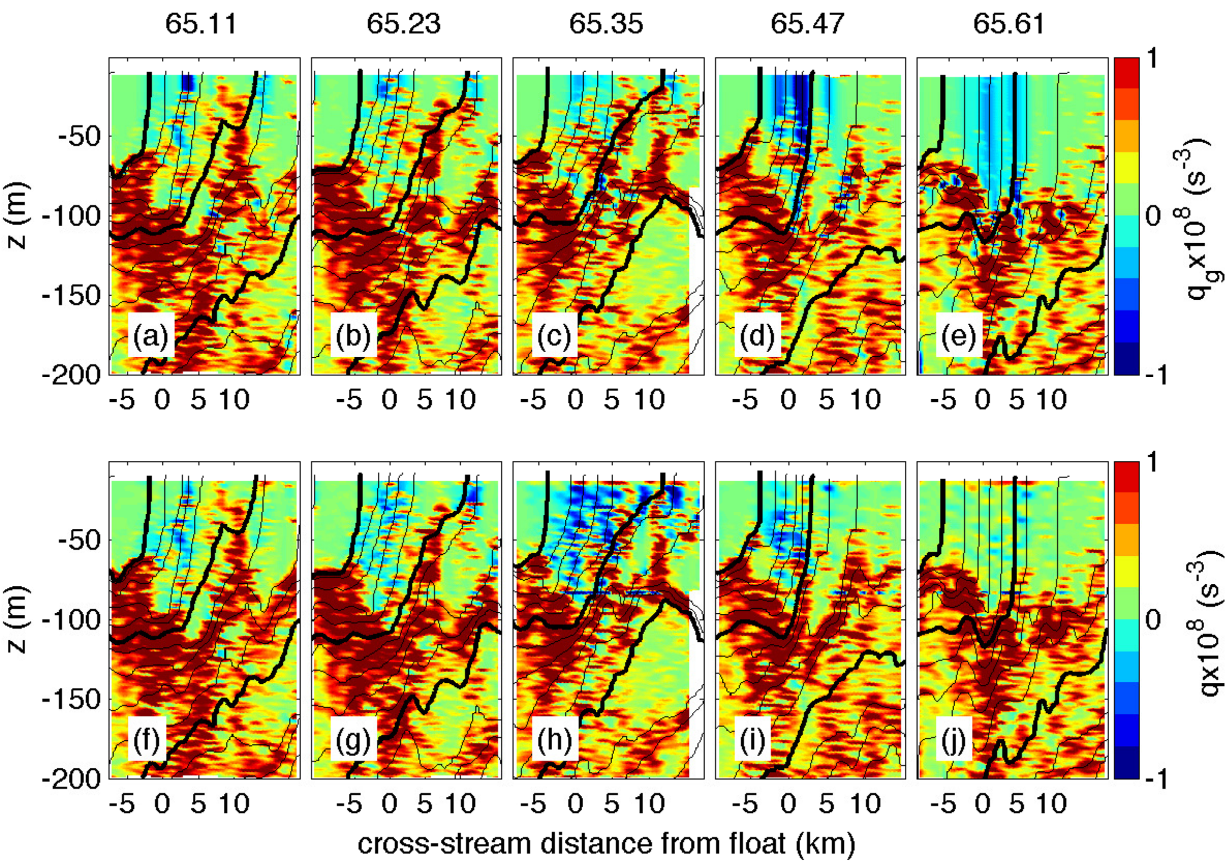

FIG. 6. Cross-stream sections of density and the PV of the geostrophic flow, $q_g = (f+\zeta)N^2 - (\partial b/\partial y)^2/f$, (top row), and of the full flow, q, (bottom row) from *R/V Atlantis* sections. Density is contoured as in Fig. 2 and the time when the sections were taken is indicated at the top of each column.

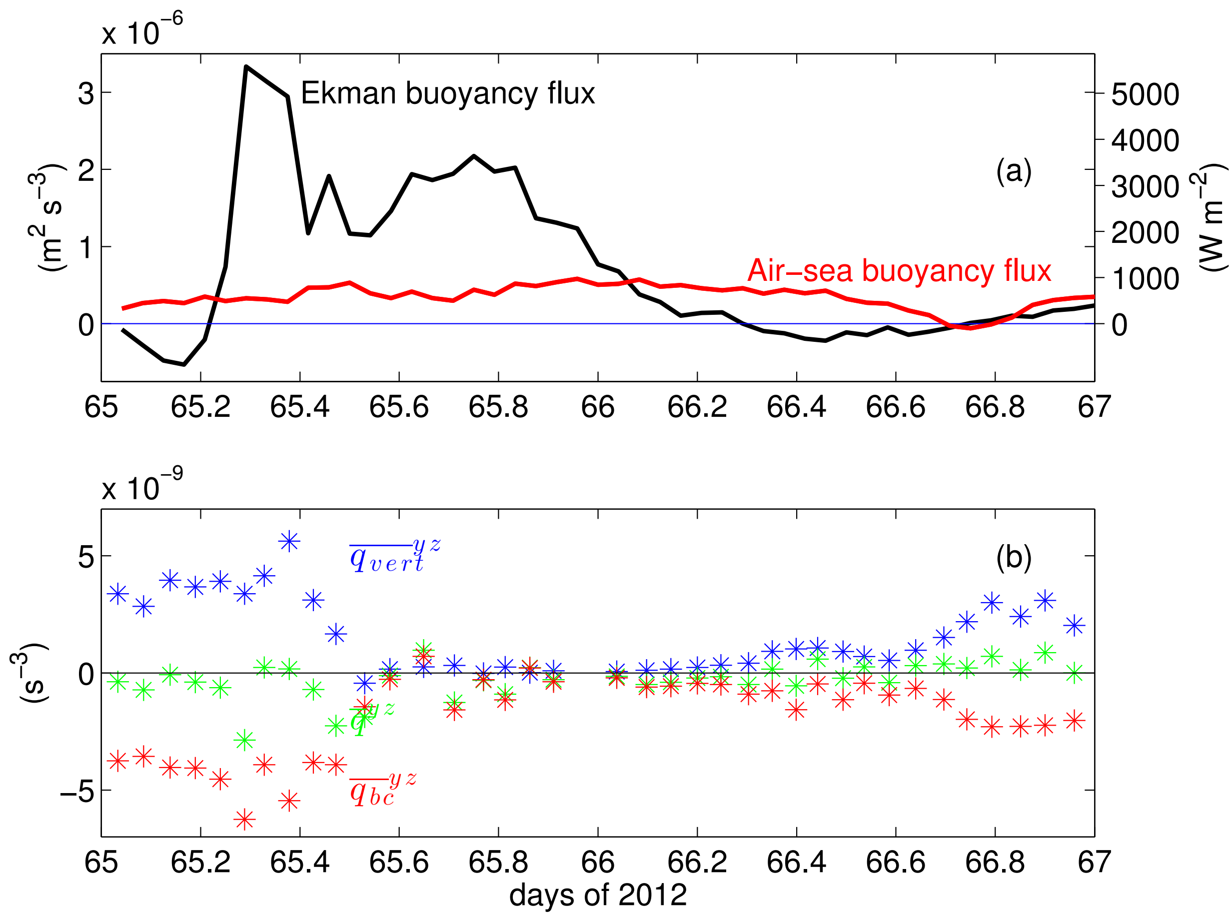

940 FIG. 7. (*a*) Time series of the the Ekman buoyancy flux, (7), (black) and the air-sea buoyancy flux (red)
941 expressed in units of a buoyancy and a heat flux on the left and right axes, respectively . Positive values in-
942 dicate destabilizing forcing. (*b*) Time series of the section-averaged PV, $\overline{q}^{yz} = \overline{q_{vert}}^{yz} + \overline{q_{bc}}^{yz}$, (green), and its
943 constituents $\overline{q_{vert}}^{yz}$ (blue) and $\overline{q_{bc}}^{yz}$ (red) based on observations from the *R/V Knorr*. The average $\overline{()}^{yz}$ was cal-
944 culated over an area that spanned the upper 60 m of the water column and between the 25.5 and 26.0 kg m^{-3}
945 isopycnals in the cross-stream direction.

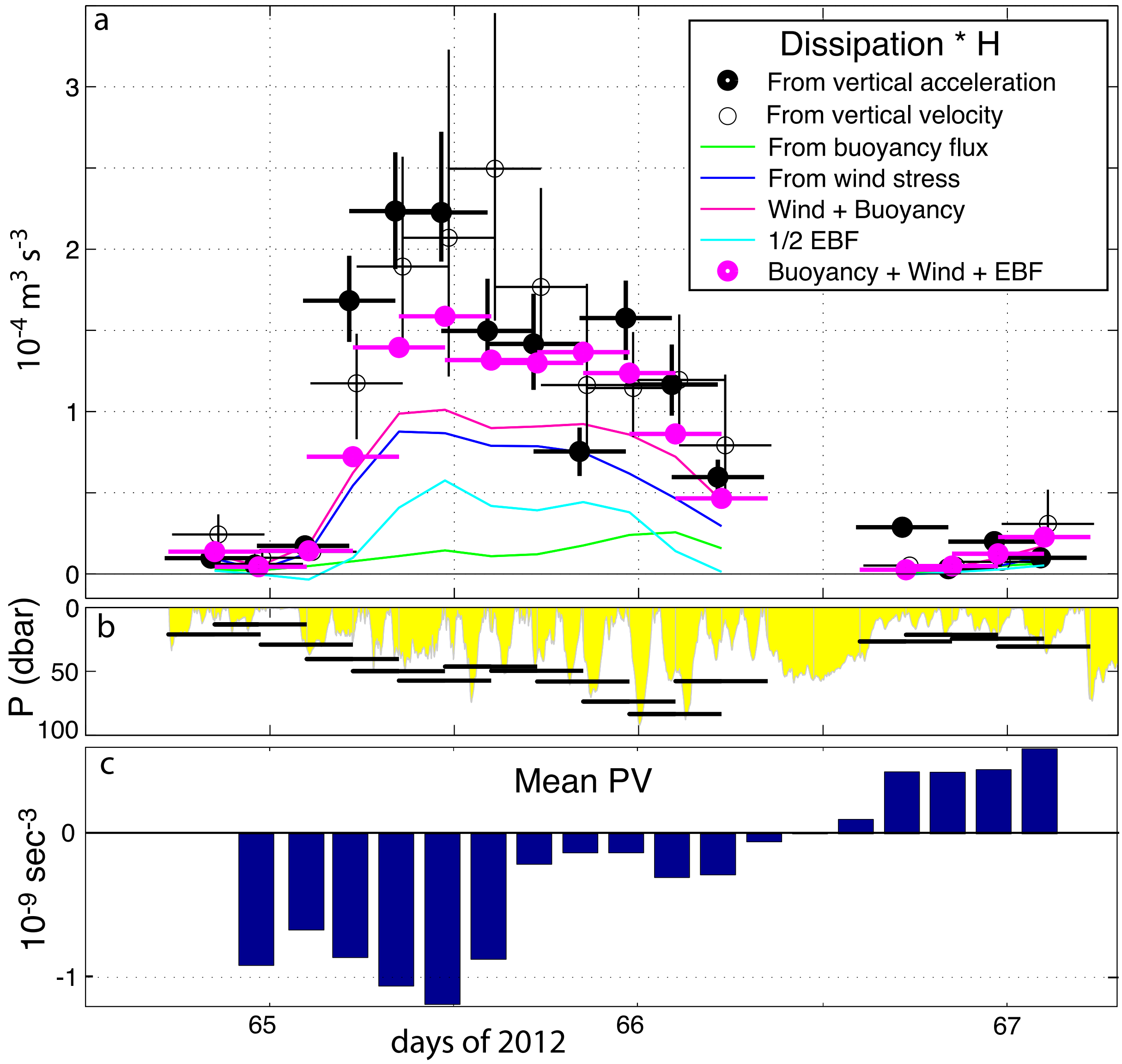

946 FIG. 8. a) Time series of boundary layer integrated dissipation estimated from float acceleration spectrum (black solid symbol) and from float vertical kinetic energy (black open symbol), and expected dissipation from various forcings: buoyancy flux (green line), wind stress (blue line), their sum (red line), EBF (equation 7, cyan line) and the sum of all forcings (magenta symbol). All quantities are computed on half-overlapping 6 hour-long time windows. No computations were made near yearday 66.5 as float appears to be below the boundary layer. b) Float depth during Lagrangian drifts (yellow filled) and boundary layer depth for each time window (heavy black) estimated as twice the mean float depth. c) Time series of the section-averaged PV, $\overline{q}^{yz}$.

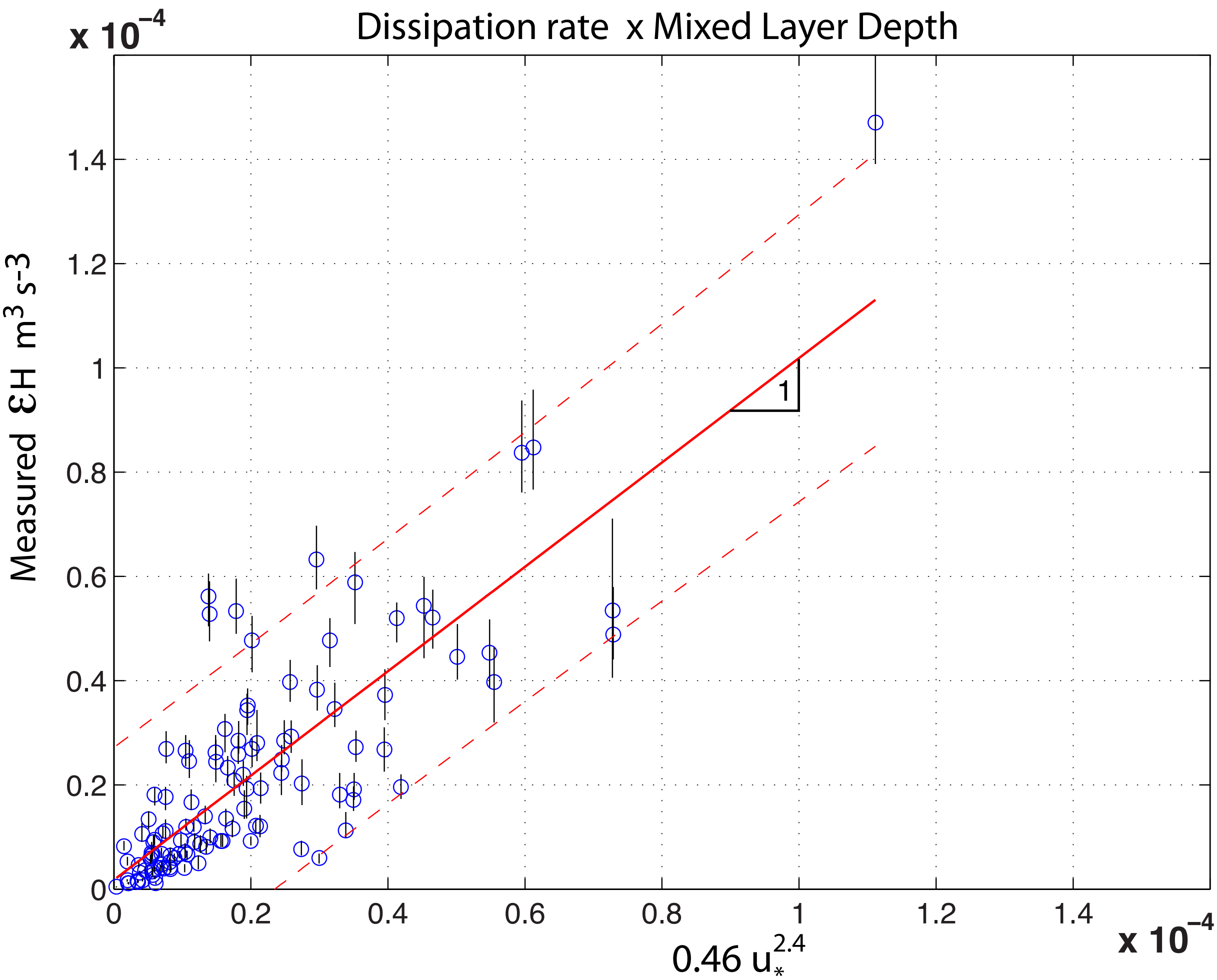

953 FIG. 9. Depth integrated dissipation rate measured by Lagrangian floats deployed near Ocean Station P (145W, 50N, D'Asaro et al. (2014)), vertical axis, parameterized by wind stress using (9), horizontal axis. Lines on each data point are 95% confidence limits. Solid red line has a slope of 1. Dashed red lines are two standard deviations of the data around the line.

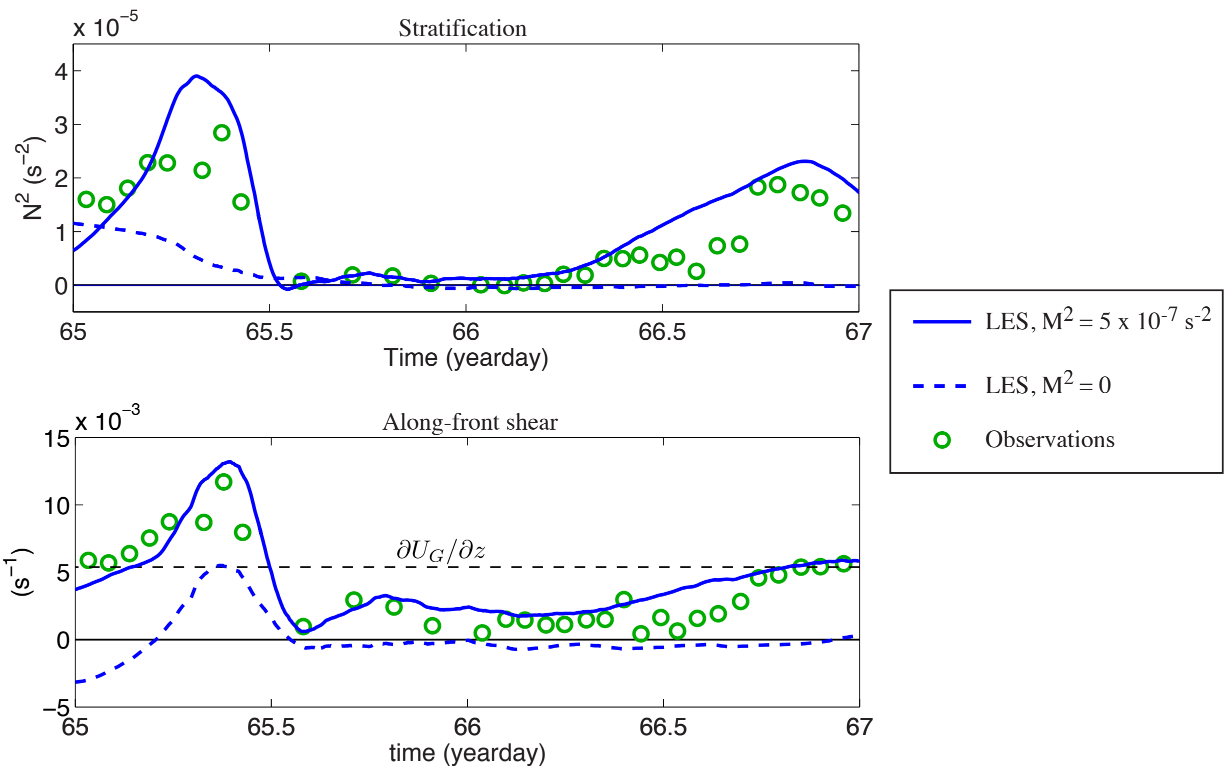

FIG. 10. Time series of the stratification (top panel) and vertical shear in the down-stream direction averaged laterally across the domain and from $-5\text{m} < z < -60\text{m}$ in the vertical for the LES with (solid blue line) and without (dashed blue line) a front. The observed section-averaged shear and stratification (e.g. Figure 4b-c) are plotted (green circles) for comparison. The value of the thermal wind-shear used in the LES with the front indicated is indicated by the black dashed line in the bottom panel.

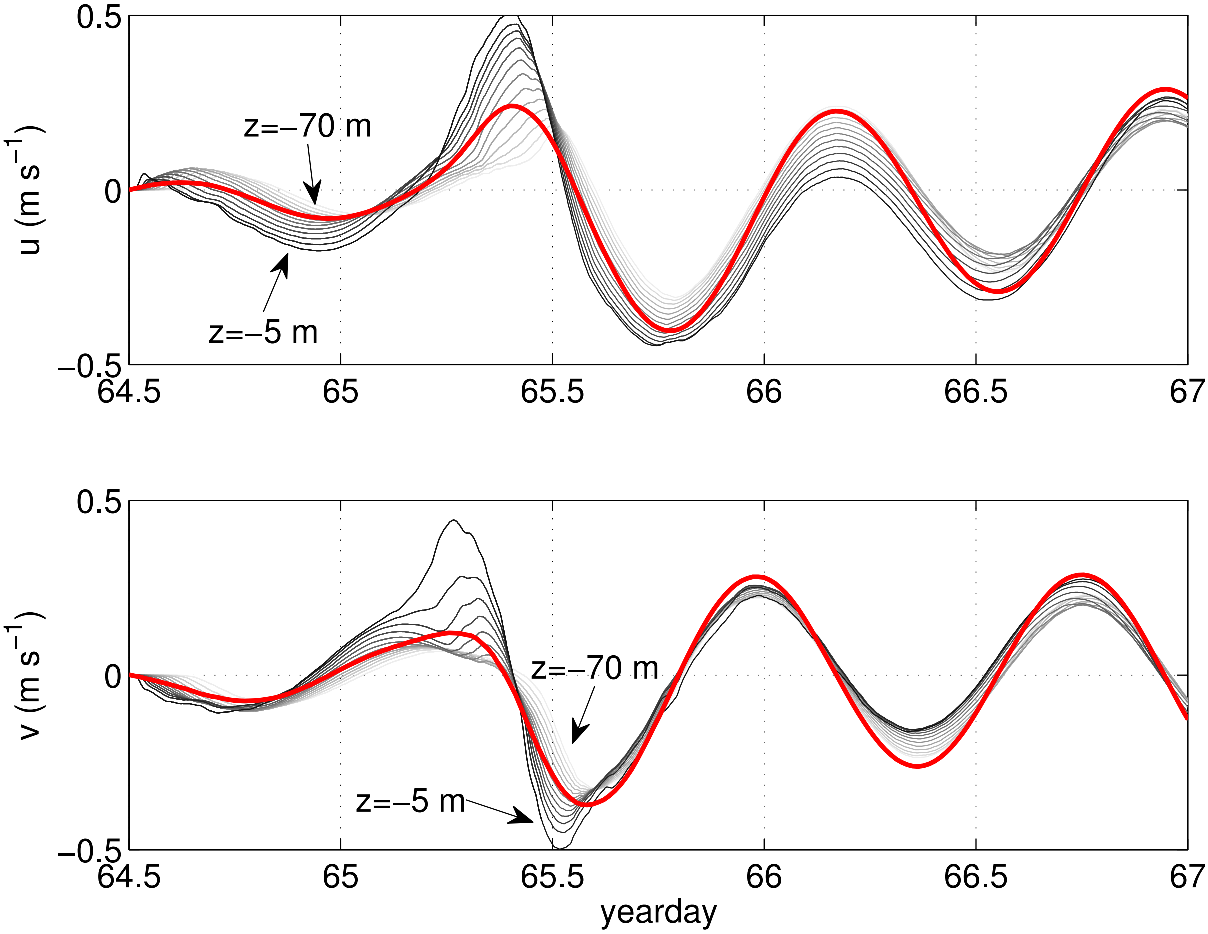

FIG. 11. Time series of the down-stream (top panel) and cross-stream (bottom panel) components of the ageostrophic flow averaged laterally over the frontal zone evaluated from 70 m to 5 meters below the surface (lines in grayscale plotted every 5m, with lighter shades corresponding to greater depths). The depth-averaged velocity associated with inertial motions forced by the observed winds, i.e. solutions to (10) and (11), (U_i, V_i), is denoted by the red line.

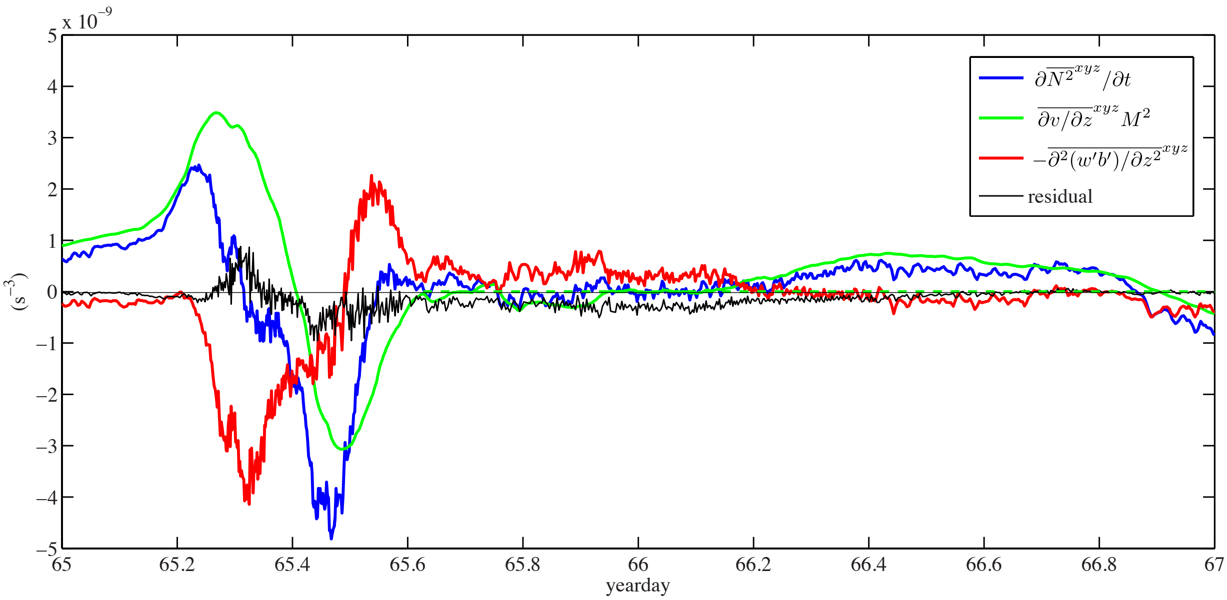

FIG. 12. Terms in the laterally and vertically averaged stratification budget (12), i.e. $\partial \overline{N^2}^{xyz}/\partial t$ (blue), differential horizontal advection (DHAV, green), and differential mixing (N2MIX, red) diagnosed from the LES with $M^2 \neq 0$. The average used to construct the budget runs across the lateral width of the domain and between -60 m $\leq z \leq -5$ m in the vertical. The residual of the budget is plotted in black.

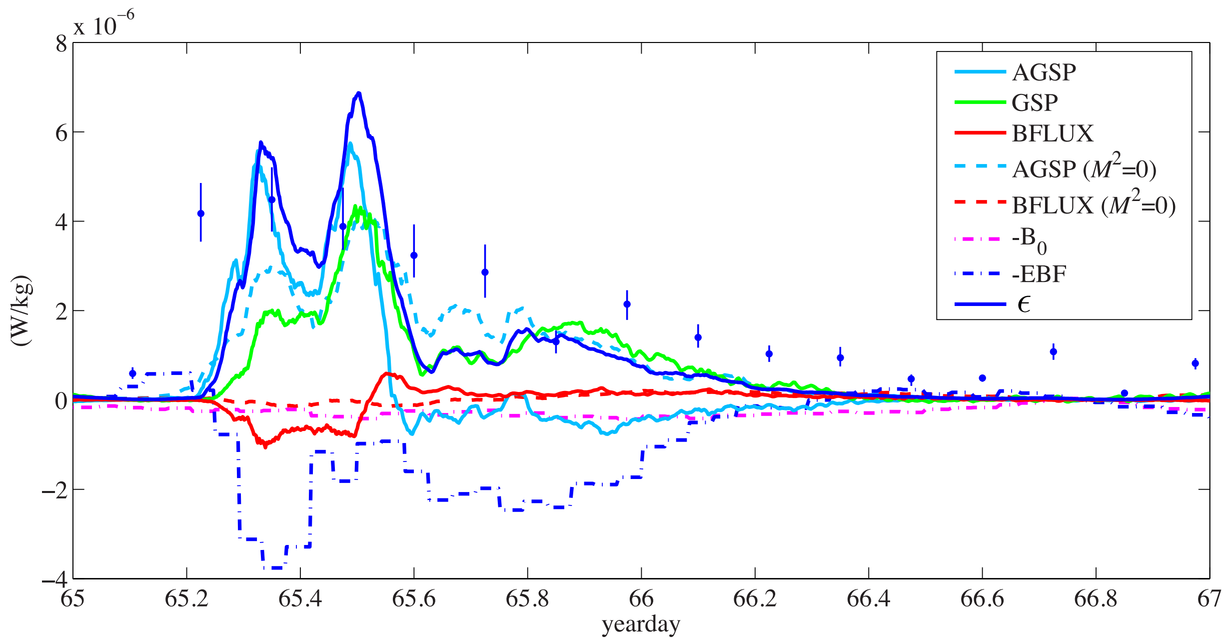

FIG. 13. Timeseries of the geostrophic shear production (GSP) buoyancy flux (BFLUX) and ageostrophic shear production (AGSP) from the simulation forced with observed winds and buoyancy flux with a front (solid) and without a front (dashed). The dissipation, ε, from the simulation with a front (dark blue line) is also shown. Each term is averaged over the horizontal extent of the domain and from $-60\text{m} < z < -5\text{m}$. For reference, dot-dashed lines show the Ekman buoyancy flux (EBF) and the surface buoyancy flux, B_0, (note that both quantities have been multiplied by -1 to avoid having too many overlapping curves on the figure). Solid blue circles show the mean boundary layer dissipation estimated from the Lagrangian float acceleration spectrum, along with 95% confidence intervals.

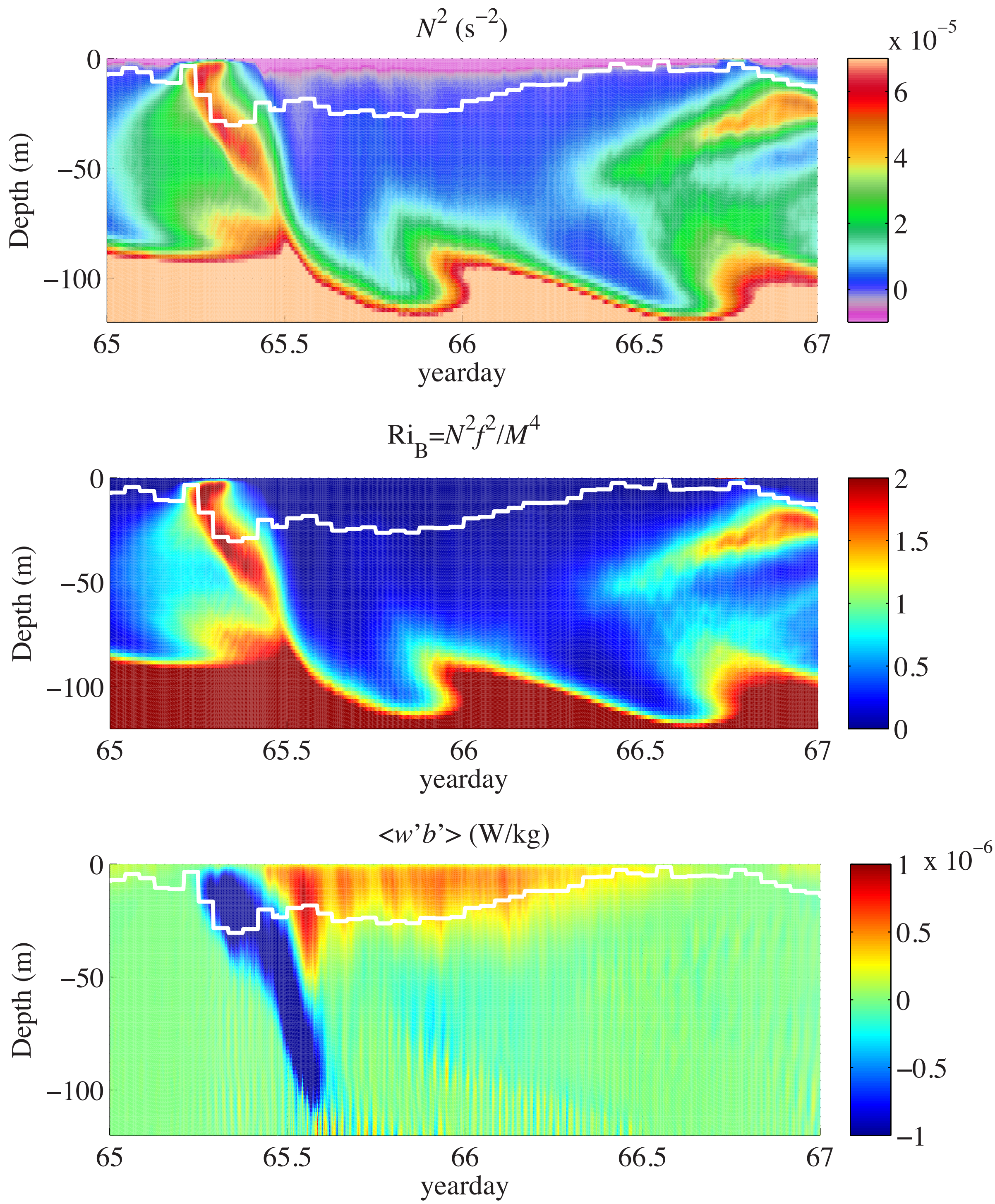

FIG. 14. Time series of the squared buoyancy frequency, N^2 (top panel), Richardson number of the geostrophic flow (middle panel), and buoyancy flux (bottom panel), from the LES with a front. All variables have been averaged laterally across the domain. The predicted convective layer depth, h, calculated from the instantaneous surface fluxes is indicated by a white line in each panel.

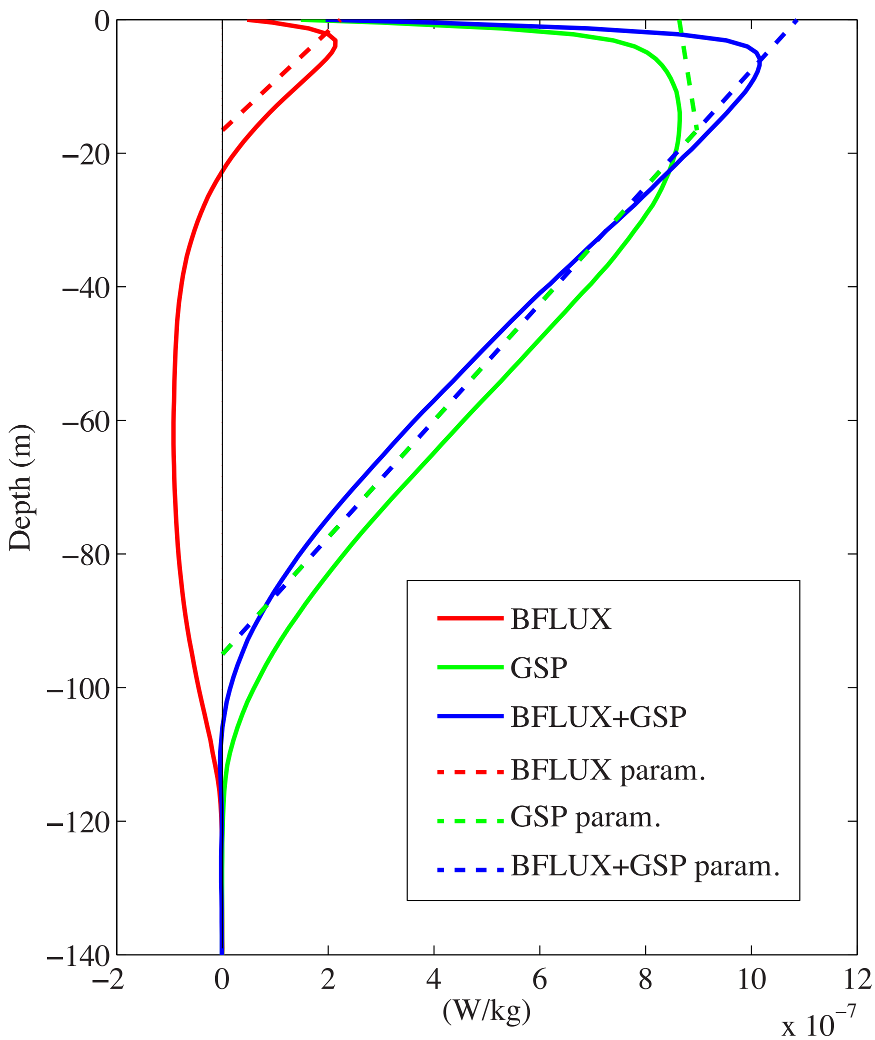

FIG. 15. Terms in the TKE budget diagnosed from the LES with a front averaged over three inertial periods starting at yearday 64.5 (solid lines). The parameterizations for the buoyancy flux, geostrophic shear production, and their sum are indicated by the dashed red, green, and blue lines, respectively.

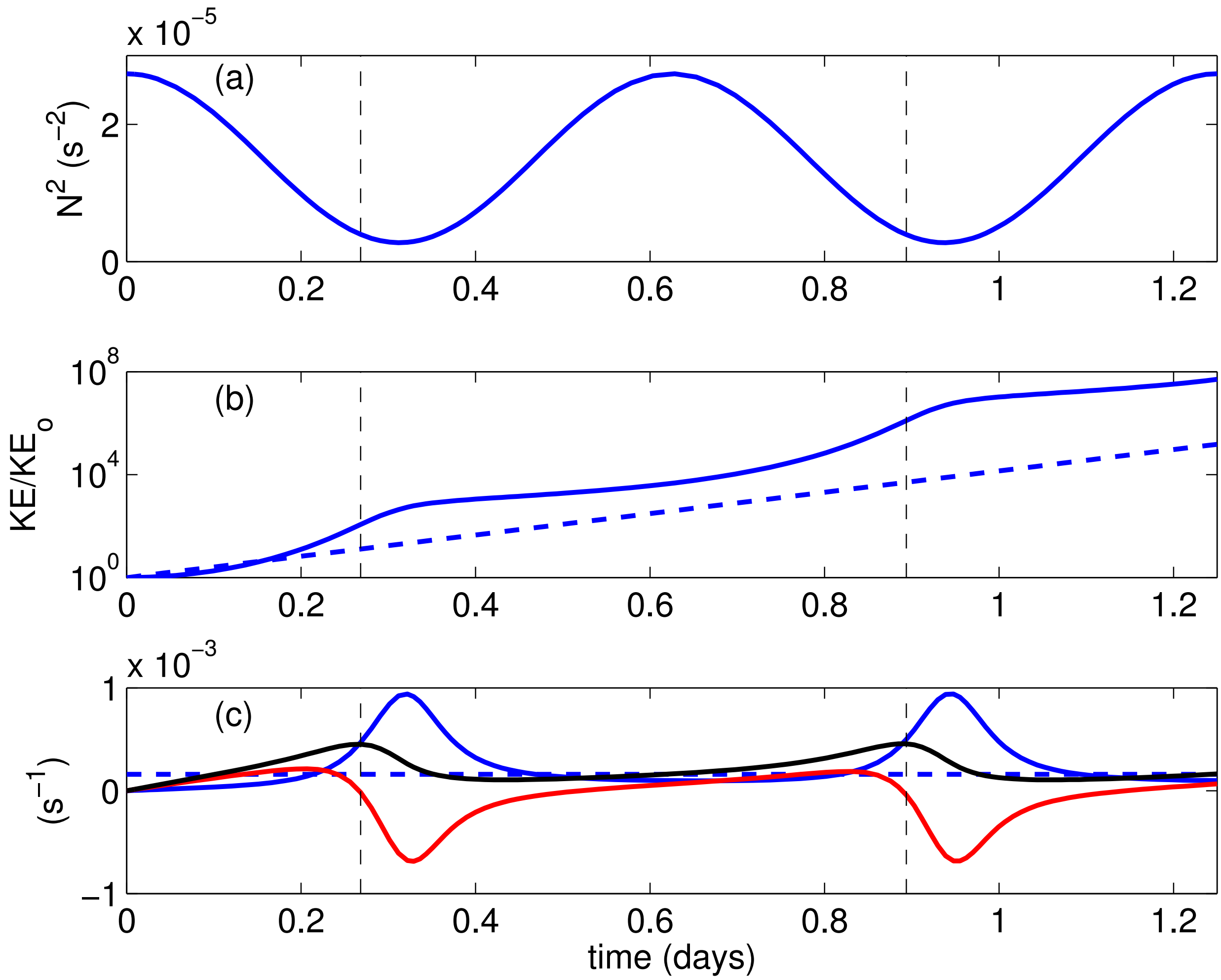

FIG. 16. (*a*) Time series of the stratification of the basic state used in the stability analysis. (*b*) The KE of a perturbation to this basic state with flow that is constrained to run parallel to isopycnals (solid line). The KE of SI in a basic state without an inertial oscillation but with the same PV is also shown in the panel (dashed line). (*c*) Terms in the perturbation KE equation (24) for the basic state with an inertial oscillation expressed in units of a growth rate: GSP/KE (solid blue line), $AGSP/KE$ (red line), and $(GSP+AGSP)/KE$ (black line). The growth rate of the SI that develops in the basic state without the inertial oscillation is indicated by the blue dashed line. The vertical dashed lines in each panel denote the times when the perturbation experiences explosive growth, i.e. when $(GSP+AGSP)/KE$ is maximum.

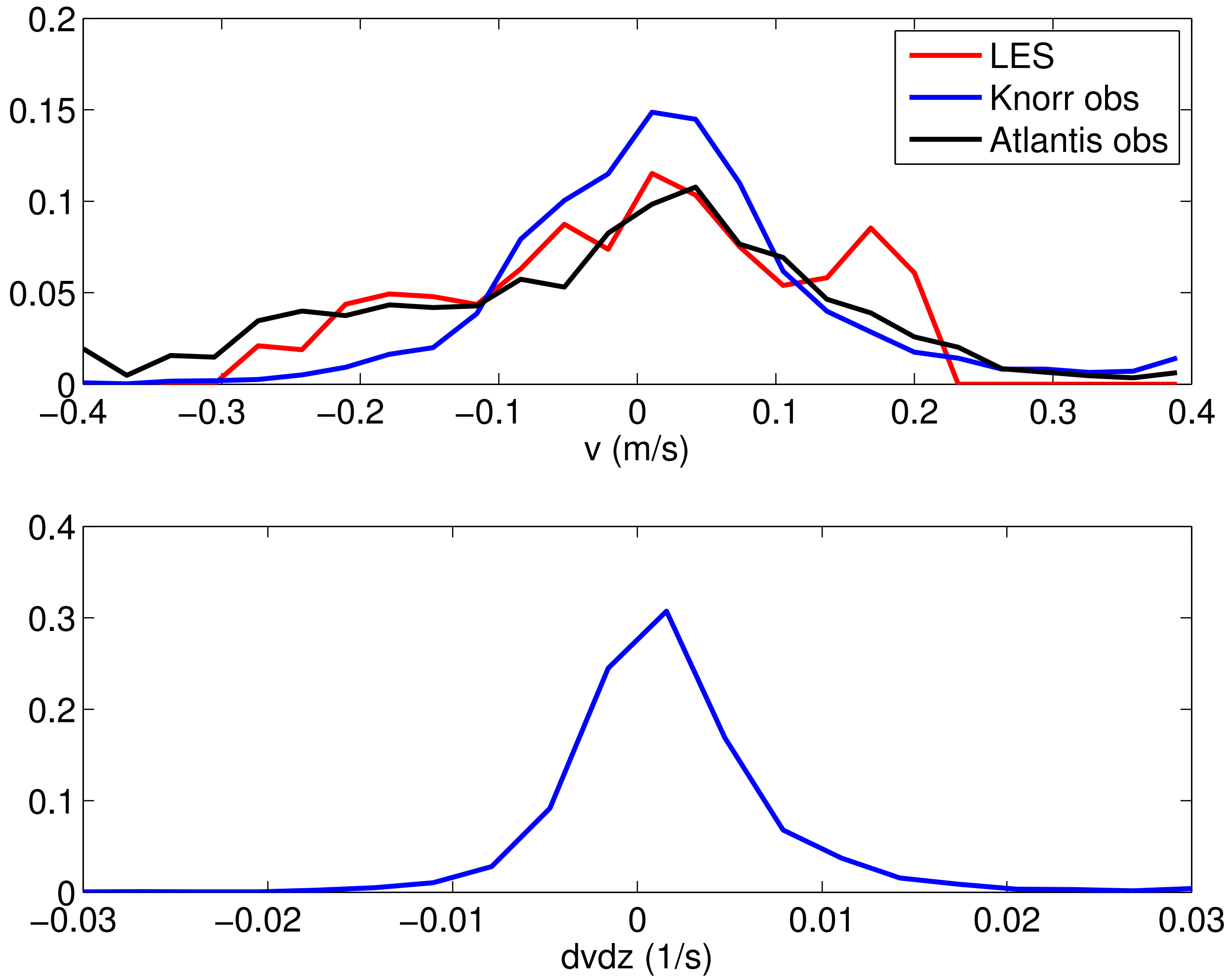

FIG. 17. Histograms of the cross-stream velocity, v, from the observations and LES (top panel) and the vertical shear of the cross-stream velocity $\partial v/\partial z$ from the observations (bottom panel). The standard deviation of v from the Knorr observations and the LES are both 0.12 m s^{-1} while for the Atlantis observations it is 0.17 m s^{-1}. The mean of $\partial v/\partial z$ is 0.0016 s^{-1}.